

Top Yukawa coupling measurement at the muon collider

Miranda Chen[†] and Da Liu^{✉*}

*Center for Quantum Mathematics and Physics (QMAP), University of California-Davis,
Davis, California 95616, USA*

 (Received 13 January 2023; accepted 5 March 2024; published 11 April 2024)

We have presented a detailed study about the prospects for the measurement of the top Yukawa coupling in the vector boson fusion production of a top quark pair at high energy muon colliders. By employing the effective W approximation and the high energy limit for the helicity amplitudes of the subprocess $W^+W^- \rightarrow t\bar{t}$, we have derived the energy scaling of the statistical signal significance in the presence of the anomalous couplings by focusing on the interference term only. The sensitivity on the top Yukawa coupling decreases as the bin energy increases. For the anomalous triple gauge boson couplings and the gauge-boson-fermion couplings with E^2 energy growing behavior, the signal significance has mild increase at the beginning and starts to decrease for $\hat{s}_{t\bar{t}} \sim 0.2s_{\mu^+\mu^-}$. The 95% CL on the anomalous top Yukawa coupling is projected to be 5.6% (1.7%) at a 10 (30) TeV muon collider, which is comparable to the sensitivity of 2% at the 100 TeV collider.

DOI: [10.1103/PhysRevD.109.075020](https://doi.org/10.1103/PhysRevD.109.075020)

I. INTRODUCTION

Precision measurement and direct resonance searches are the two main ways to search for new physics at colliders. In the first category, we usually perform the measurement at the pole masses of known particles such as the Z boson and Higgs boson [1,2]. The precision that can be achieved is limited by the systematic and statistical uncertainties. In the second method, we look for the peak in the invariant mass distribution or other kinematical variables of the decay products of new particles, which directly probes the energy scale of the mass of the new heavy particles. However, it has long been noticed that any modifications to the couplings predicted by the spontaneously broken gauge theories will lead to some kind of energy growing behaviors that violate tree-level unitarity [3] (see [4] recently for the on shell derivation). Specific to $2 \rightarrow 2$ scattering, this means that anomalous couplings will lead to energy growing behaviors rather than a constant, as one would expect in the Standard Model (SM). It is well known that $W_L W_L \rightarrow W_L W_L$ scattering processes will grow like E^2 in the high energy limit for nonstandard Higgs gauge boson couplings. On the other hand, $W_L W_L \rightarrow f\bar{f}$ processes will grow like E^2 for anomalous gauge-boson fermion

couplings and anomalous triple gauge boson couplings (aTGCs). It will also grow linearly with E in the case of non-Standard Higgs Yukawa couplings. This has motivated the precision measurements at the hadron colliders [5–8] due to the high energy bins available at the LHC.

Recently, there is a growing interest in the high energy muon collider [9,10] and active researches are currently being done to explore the physics potential [11–40]. The attractiveness of a muon collider lies in its availability to reach high energy $\gtrsim 10$ TeV while keeping the systematical uncertainty under control. It can potentially achieve high integrated luminosity as follows:

$$L = \left(\frac{\sqrt{s_\mu}}{10 \text{ TeV}} \right)^2 \times 10 \text{ ab}^{-1}. \quad (1)$$

This will allow percentage-level precision in the high energy bin of $\gtrsim 10$ TeV for muon annihilation electroweak processes with final states of difermions and dibosons [33], which is essentially probing the 100 TeV scale. Note that this is higher than the flavor physics scale in the composite Higgs scenarios [41,42]. The high energy muon collider can also be considered as a gauge boson collider due to the logarithmic growth of the electroweak gauge boson parton distribution functions [12,14,26]. In this paper, we take $\mu^+\mu^- \rightarrow t\bar{t}\nu\bar{\nu}$ at high energy muon collider as an example to illustrate the extent to which the energy growing behaviors in the vector boson fusion subprocess can help to measure anomalous couplings. We will employ the effective W -boson approximation (EWA) [43–45] with the analytical formulas of the helicity amplitudes for the subprocess $W^+W^- \rightarrow t\bar{t}$ to analyze the energy scaling behavior of the

*Corresponding author: daeliu@ucdavis.edu

[†]mwqchen@ucdavis.edu

Published by the American Physical Society under the terms of the Creative Commons Attribution 4.0 International license. Further distribution of this work must maintain attribution to the author(s) and the published article's title, journal citation, and DOI. Funded by SCOAP³.

signal significance. After the semianalytical study, we will move on to study the prospects for the measurement of the top Yukawa coupling at the 10 TeV and 30 TeV muon collider, where we are focusing on the semileptonically decaying channel of the top quark pair.

The paper is organized as follows. In Sec. II, we perform a generic energy scaling analysis of signal significance for vector boson fusion processes in the presence of anomalous couplings at the high energy muon colliders. In particular, we give a detailed analysis for the $W^+W^- \rightarrow t\bar{t}$ process and study the high energy and threshold behaviors for the helicity amplitudes in the presence of anomalous top Yukawa coupling, aTGCs, and anomalous gauge-boson-fermions couplings. In Sec. III, we study the prospects on the top Yukawa coupling measurement in the vector boson fusion (VBF) production of $t\bar{t}$ at the high energy muon collider. For future possible study, we have also performed a brief analysis about the top Yukawa coupling measurement in the VBF production of $t\bar{t}h$. The results are presented in the Sec. IV. Section V contains our conclusion.

II. GENERAL ANALYSIS OF WEAK BOSON FUSION PROCESSES

In this section, we will study the energy scaling behavior of S/\sqrt{B} and S/B in the presence of anomalous couplings for the weak boson fusion processes in the two particle final states at the high energy muon collider. We will focus on the hard scattering regime where the scattering angle is in the central region, i.e., $-\hat{t} \sim \hat{s} = \hat{E}^2$. We start from the analysis of the partonic processes $VV \rightarrow XY$ and then employ the EWA to analyze the energy scaling at the $\mu^+\mu^-$ collider.

A. Energy scaling behavior in $W^+W^- \rightarrow XX, ZZ \rightarrow XX, WZ \rightarrow XY$

As a preliminary step to understanding the energy scaling behavior of processes at a muon collider, we consider the simpler problem of $VV \rightarrow XY$ where the V stands for a W or Z boson and X, Y can be any SM particles with electroweak charges such that the processes have nonzero tree-level contributions. Restricting to $2 \rightarrow 2$ processes where the initial state contains two massive bosons, we can express our cross sections schematically in terms of amplitudes as

$$\sigma_{\text{int}} \sim \frac{\mathcal{M}_{\text{SM}}\mathcal{M}_{\delta_i}}{\hat{E}^2}; \quad \sigma_{\text{SM}} \sim \frac{\mathcal{M}_{\text{SM}}^2}{\hat{E}^2}, \quad (2)$$

where \mathcal{M}_{SM} refers to the SM amplitude and \mathcal{M}_{δ_i} refers to amplitudes containing beyond Standard Model (BSM) physics. Since we only focus on the energy scaling behavior of the cross sections in this section, we have neglected the possible complex phases and the angular dependence of the amplitudes. Note that we also study the hard scattering regime which is away from the possible scattering angle singularities (mainly from t channel or u channel). In our

semianalytical analysis, we assume that the BSM linear contribution dominates over the pure BSM cross section (quadratic contribution), which is usually the case in order for the effective field theory (EFT) expansion to make sense in a weakly coupled theory. In the Standard Model effective field theory (SMEFT) language, pure BSM cross sections should be considered as the same level as the dimension-eight contribution. This assumption is equivalent to the statement that the leading effects are coming from the dimension-six level.¹ Then given our processes, \mathcal{M}_{δ_i} is linear in the anomalous couplings δ_i , and we see that σ_{int} is the interference term. We start from the analysis by assuming that we can exactly measure the helicities of the initial bosons and final state particles, so we are really considering

$$\frac{S^{h_1\dots h_4}}{\sqrt{B^{h_1\dots h_4}}}, \quad (3)$$

where the signal in the helicity configuration $S^{h_1\dots h_4}$ is linear in the coupling modifier δ_i . In what follows, we only consider the SM process $VV \rightarrow XY$ as our dominant background. It is straightforward to see that under our simplified assumption, for the case where statistical error dominates, the dependence on the SM amplitude of the statistical significance cancels out:

$$\frac{S^{h_1\dots h_4}}{\sqrt{B^{h_1\dots h_4}}} \sim \frac{\sigma_{\text{int}}^{h_1\dots h_4}}{\sqrt{\sigma_{\text{SM}}^{h_1\dots h_4}}} \sim \frac{\mathcal{M}_{\delta_i}^{h_1\dots h_4}}{\hat{E}}. \quad (4)$$

Note that we have neglected all the constant factors, like the integrated luminosity. Then we can see that in order for the significance to grow with energy, \mathcal{M}_{δ_i} must be at least quadratic in \hat{E} . This is certainly true for the Higgs gauge boson coupling modification in the vector boson scattering processes $V_L V_L \rightarrow V_L V_L$ and for the anomalous gauge boson fermion coupling in the $V_L V_L \rightarrow f\bar{f}$ processes. However for the top Yukawa coupling, we only have linear energy growing behavior, and we expect that the significance stays constant as the bin energy increases. This does not mean the high energy bins are completely irrelevant, as one can still improve the significance by combing all the energy bins.

In reality, we cannot measure the helicities of the final states exactly, and there is always contamination from other helicity categories. At the muon collider, it will likely be difficult to determine the initial gauge boson helicities, especially for the W^\pm bosons. We now consider the inclusive case, where we sum over the cross sections from all the helicity configurations for the initial and final states. In this fully inclusive case, the statistical significance scales like

¹In the strong multipole interaction scenario considered in Ref. [46], there exists an energy window that the squared term dominates over the linear term, which is also consistent with EFT expansion. We will not pursue this case in this paper.

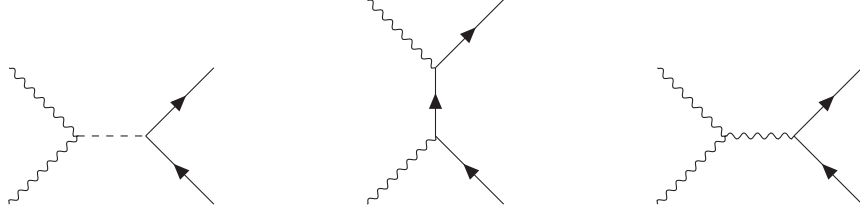


FIG. 1. Tree-level diagrams for $W^+W^- \rightarrow t\bar{t}$. The gauge boson propagator in the last diagrams can be either Z or γ .

$$\frac{S}{\sqrt{B}} \sim \frac{\sum_{h_1 \dots h_4} \sigma_{\text{int}}^{h_1 \dots h_4}}{\sqrt{\sum_{h_1 \dots h_4} \sigma_{\text{SM}}^{h_1 \dots h_4}}} \sim \frac{1}{\hat{E}} \sum_{h_1 \dots h_4} \mathcal{M}_{\text{SM}}^{h_1 \dots h_4} \mathcal{M}_{\delta_i}^{h_1 \dots h_4}, \quad (5)$$

where we have used the fact the inclusive SM cross section has the following energy scaling:

$$\sum_{h_1 \dots h_4} \sigma_{\text{SM}}^{h_1 \dots h_4} \sim \frac{1}{\hat{E}^2}. \quad (6)$$

We can see that in order for the significance to increase with energy, not only should the BSM helicity amplitude $\mathcal{M}_{\delta_i}^{h_1 \dots h_4}$ grow as \hat{E}^2 , but the corresponding linearly mixing term $\mathcal{M}_{\text{SM}}^{h_1 \dots h_4}$ should also stay constant as the energy increases.² Before studying the energy scaling of the weak boson parton luminosity in detail, we comment on the systematic uncertainty. If the systematic error dominates, the signal significance becomes

$$\frac{S^{h_1 \dots h_4}}{B^{h_1 \dots h_4}} \sim \frac{\sigma_{\text{int}}^{h_1 \dots h_4}}{\sigma_{\text{SM}}^{h_1 \dots h_4}} \sim \frac{\mathcal{M}_{\delta_i}^{h_1 \dots h_4}}{\mathcal{M}_{\text{SM}}^{h_1 \dots h_4}}, \quad (7)$$

while for the inclusive case, it reads as

$$\frac{S}{B} = \frac{\sum_{h_1 \dots h_4} \sigma_{\text{int}}^{h_1 \dots h_4}}{\sum_{h_1 \dots h_4} \sigma_{\text{SM}}^{h_1 \dots h_4}} \sim \sum_{h_1 \dots h_4} \mathcal{M}_{\text{SM}}^{h_1 \dots h_4} \mathcal{M}_{\delta_i}^{h_1 \dots h_4}. \quad (8)$$

In the exclusive case, since the SM helicity amplitudes $\mathcal{M}_{\text{SM}}^{h_1 \dots h_4}$ are at most a constant for the $2 \rightarrow 2$ processes, any energy growing behavior in the BSM amplitude $\mathcal{M}_{\delta_i}^{h_1 \dots h_4}$ will lead to enhancement of the signal significance at high energy bins. This is especially the case at the hadron colliders like LHC, as one generally has large systematic errors ranging from a few percentages to tens of percentages. For the inclusive case, similar to the statistical uncertainty dominance, we need both $\mathcal{M}_{\delta_i}^{h_1 \dots h_4}$ to increase with energy and $\mathcal{M}_{\text{SM}}^{h_1 \dots h_4}$ to not decrease too quickly.

²When taking into account the angular distributions of the decayed products of final particles, the requirement may be relaxed as different helicity configurations of XY can interfere with each other [47,48].

B. Anatomy of $W^+W^- \rightarrow t\bar{t}$

In this subsection, we focus on the VBF production of the top pair and study in detail the helicity amplitudes of the subprocess $W^+W^- \rightarrow t\bar{t}$ in the presence of anomalous couplings. The relevant Feynman diagrams are shown in Fig. 1. For completeness and also for future possible studies, we also include the aTGCs, the gauge boson fermion couplings, and Higgs gauge boson coupling. The full formulas and the conventions are presented in Appendix B (see Refs. [49,50] for $tW \rightarrow tW$ helicity amplitudes). Here we discuss their high energy and threshold behaviors. We start from the high energy hard scattering limit and consider the central region, where $1 \pm \cos \theta$ is large enough to justify our expansion. As before, we denote $\hat{E} = \sqrt{\hat{s}}$. The results for the helicity-conserving configurations of the top quarks, i.e., $(h_t, h_{\bar{t}} = (\pm \frac{1}{2}, \mp \frac{1}{2}))$ are listed in Table I, while the results for the helicity-violating configurations i.e., $(h_t, h_{\bar{t}} = (\pm \frac{1}{2}, \pm \frac{1}{2}))$ are presented in Table II. The energy scaling for the helicity partonic cross section and the exclusive statistical significance is given in Table III. Several comments are in order. First, for the SM helicity amplitudes, only the following helicity configurations survive in the high energy limit:

$$(h_{W^+}, h_{W^-}, h_t, h_{\bar{t}}) = \left(\pm 1, \mp 1, -\frac{1}{2}, \frac{1}{2} \right), \left(0, 0, \mp \frac{1}{2}, \pm \frac{1}{2} \right), \\ \left(-1, 0, -\frac{1}{2}, -\frac{1}{2} \right), \left(0, 1, \frac{1}{2}, \frac{1}{2} \right). \quad (9)$$

The results can be understood by using the Goldstone equivalence theorem and by working in the electroweak-symmetry-unbroken phase of the SM where the Goldstone scalars ϕ_{\pm} appear as external states and the SM gauge bosons and top quarks are massless particles. For the longitudinal W^{\pm} boson processes, we can see that the $SU(2)_L \times U(1)_Y$ quantum numbers of the top quarks appear in the helicity amplitudes:

$$T_3^L(t_{L,R})g^2 + Y(t_{L,R})g^2, \quad (10)$$

where T_3^L is the third weak isospin generator and Y is the hypercharge. The presence of the SM top Yukawa coupling squared term m_t^2/v^2 associated with the t -channel pole in

TABLE I. High energy limit of the helicity amplitude for $W^+W^- \rightarrow t\bar{t}$ with $h_t - h_{\bar{t}} = \mp 1$. Here m_{SM} denotes m_W , m_t , m_h .

$(h_t h_{\bar{t}})$	$(h_{W^+} h_{W^-})$	$\tilde{\mathcal{M}}_{h_{W^+} h_{W^-}; h_t h_{\bar{t}}}^{\text{SM}}$	$\tilde{\mathcal{M}}_{h_{W^+} h_{W^-}; h_t h_{\bar{t}}}^{\text{BSM}}$
$(-\frac{1}{2} \frac{1}{2})$	$(+1 -1), (-1 +1)$	$i \frac{g^2}{-1+\cos\theta}$	$\mathcal{O}(\delta_{Wtb})$
	$(+1 +1), (-1 -1)$	$\mathcal{O}(\frac{m_{\text{SM}}^2}{E^2})$	$i \frac{g^2 \hat{E}^2 (3\lambda_Z + 4s_W^2 (\lambda_\gamma - \lambda_Z))}{6\sqrt{2}m_W^2}$
	$(+1 0), (0 -1)$	$\mathcal{O}(\frac{m_{\text{SM}}}{E})$	$\mathcal{O}\left(\frac{\hat{E}}{m_{\text{SM}}} (\delta g_1^Z, \delta\kappa_{Z,\gamma}, \delta_{Wtb}, \delta_{Z_{1L}}, \lambda_{Z,\gamma})\right)$
	$(-1 0), (0 +1)$	$\mathcal{O}(\frac{m_{\text{SM}}}{E})$	$\mathcal{O}\left(\frac{\hat{E}}{m_{\text{SM}}} (\delta g_1^Z, \delta\kappa_{Z,\gamma}, \delta_{Wtb}, \delta_{Z_{1L}}, \lambda_{Z,\gamma})\right)$
	$(0 0)$	$i \frac{3g^2 + g'^2}{6\sqrt{2}}$	$i \frac{g^2 \hat{E}^2}{6\sqrt{2}m_W^2} ((-3 + 4s_W^2)(\delta\kappa_Z + \delta_{Z_{1L}}) + 6\delta_{Wtb} - 4s_W^2 \delta\kappa_\gamma)$
$(h_t h_{\bar{t}})$	$(h_{W^+} h_{W^-})$	$\tilde{\mathcal{M}}_{h_{W^+} h_{W^-}; h_t h_{\bar{t}}}^{\text{SM}}$	$\tilde{\mathcal{M}}_{h_{W^+} h_{W^-}; h_t h_{\bar{t}}}^{\text{BSM}}$
$(\frac{1}{2} - \frac{1}{2})$	$(+1 -1), (-1 +1)$	$\mathcal{O}(\frac{m_{\text{SM}}^2}{E^2})$	$\mathcal{O}(\frac{m_{\text{SM}}^2}{E^2})$
	$(+1 +1), (-1 -1)$	$\mathcal{O}(\frac{m_{\text{SM}}^2}{E^2})$	$i \frac{\sqrt{2}g^2 s_W^2 \hat{E}^2 (\lambda_\gamma - \lambda_Z)}{3m_W^2}$
	$(+1 0), (0 -1)$	$\mathcal{O}(\frac{m_{\text{SM}}}{E})$	$\mathcal{O}\left(\frac{\hat{E}}{m_{\text{SM}}} (\delta g_1^Z, \delta\kappa_{Z,\gamma}, \delta_{Z_{1R}}, \lambda_{Z,\gamma})\right)$
	$(-1 0), (0 +1)$	$\mathcal{O}(\frac{m_{\text{SM}}}{E})$	$\mathcal{O}\left(\frac{\hat{E}}{m_{\text{SM}}} (\delta g_1^Z, \delta\kappa_{Z,\gamma}, \delta_{Z_{1R}}, \lambda_{Z,\gamma})\right)$
	$(0 0)$	$i \frac{\sqrt{2}g^2}{3} + i \frac{2\sqrt{2}m_t^2}{v^2(-1+\cos\theta)}$	$i \frac{\sqrt{2}g^2 s_W^2 \hat{E}^2}{3m_W^2} (\delta\kappa_Z - \delta\kappa_\gamma + \delta_{Z_{1R}})$

TABLE II. High energy limit of the Helicity amplitude for $W^+W^- \rightarrow t\bar{t}$ with $h_t - h_{\bar{t}} = 0$. Here m_{SM} denotes m_W , m_t , m_h .

$(h_t h_{\bar{t}})$	$(h_{W^+} h_{W^-})$	$\tilde{\mathcal{M}}_{h_{W^+} h_{W^-}; h_t h_{\bar{t}}}^{\text{SM}}$	$\tilde{\mathcal{M}}_{h_{W^+} h_{W^-}; h_t h_{\bar{t}}}^{\text{BSM}}$
$(-\frac{1}{2} - \frac{1}{2})$	$(+1 -1), (-1 +1)$	$\mathcal{O}(\frac{m_{\text{SM}}}{E})$	$\mathcal{O}(\frac{m_{\text{SM}}}{E} \delta_{Wtb})$
	$(+1 +1)$	$\mathcal{O}(\frac{m_{\text{SM}}^3}{E^3})$	$\mathcal{O}(\frac{\hat{E}}{m_{\text{SM}}} \lambda_{Z,\gamma})$
	$(-1 -1)$	$\mathcal{O}(\frac{m_{\text{SM}}}{E})$	$\mathcal{O}(\frac{\hat{E}}{m_{\text{SM}}} \lambda_{Z,\gamma})$
	$(+1 0), (0 -1)$	$\mathcal{O}(\frac{m_{\text{SM}}^2}{E^2})$	$\mathcal{O}(\delta g_1^Z, \delta\kappa_{Z,\gamma}, \delta_{Wtb}, \lambda_{Z,\gamma}, \delta_{Z_{1L}}, \delta_{Z_{1R}})$
	$(-1 0)$	$i g^2 \frac{m_t}{m_W(-1+\cos\theta)}$	$\mathcal{O}(\delta g_1^Z, \delta\kappa_{Z,\gamma}, \delta_{Wtb}, \lambda_{Z,\gamma}, \delta_{Z_{1L}}, \delta_{Z_{1R}})$
	$(0 +1)$	$\mathcal{O}(\frac{m_{\text{SM}}^2}{E^2})$	$\mathcal{O}(\delta g_1^Z, \delta\kappa_{Z,\gamma}, \delta_{Wtb}, \lambda_{Z,\gamma}, \delta_{Z_{1L}}, \delta_{Z_{1R}})$
	$(0 0)$	$\mathcal{O}(\frac{m_{\text{SM}}}{E})$	$-i \frac{g^2 m_t \hat{E}}{4m_W^2} (\delta_{h_{WW}} + \delta_{thh} + \mathcal{O}(\delta\kappa_{Z,\gamma}, \delta_{Z_{1L}}, \delta_{Z_{1R}}))$
$(h_t h_{\bar{t}})$	$(h_{W^+} h_{W^-})$	$\tilde{\mathcal{M}}_{h_{W^+} h_{W^-}; h_t h_{\bar{t}}}^{\text{SM}}$	$\tilde{\mathcal{M}}_{h_{W^+} h_{W^-}; h_t h_{\bar{t}}}^{\text{BSM}}$
$(\frac{1}{2} \frac{1}{2})$	$(+1 -1), (-1 +1)$	$\mathcal{O}(\frac{m_{\text{SM}}}{E})$	$\mathcal{O}(\frac{m_{\text{SM}}}{E} \delta_{Wtb})$
	$(+1 +1)$	$\mathcal{O}(\frac{m_{\text{SM}}}{E})$	$\mathcal{O}(\frac{\hat{E}}{m_{\text{SM}}} \lambda_{Z,\gamma})$
	$(-1 -1)$	$\mathcal{O}(\frac{m_{\text{SM}}^3}{E^3})$	$\mathcal{O}(\frac{\hat{E}}{m_{\text{SM}}} \lambda_{Z,\gamma})$
	$(+1 0), (0 -1)$	$\mathcal{O}(\frac{m_{\text{SM}}^2}{E^2})$	$\mathcal{O}(\delta g_1^Z, \delta\kappa_{Z,\gamma}, \delta_{Wtb}, \lambda_{Z,\gamma}, \delta_{Z_{1L}}, \delta_{Z_{1R}})$
	$(-1 0)$	$\mathcal{O}(\frac{m_{\text{SM}}^2}{E^2})$	$\mathcal{O}(\delta g_1^Z, \delta\kappa_{Z,\gamma}, \delta_{Wtb}, \lambda_{Z,\gamma}, \delta_{Z_{1L}}, \delta_{Z_{1R}})$
	$(0 +1)$	$i g^2 \frac{m_t}{m_W(1-\cos\theta)}$	$\mathcal{O}(\delta g_1^Z, \delta\kappa_{Z,\gamma}, \delta_{Wtb}, \lambda_{Z,\gamma}, \delta_{Z_{1L}}, \delta_{Z_{1R}})$
	$(0 0)$	$\mathcal{O}(\frac{m_{\text{SM}}}{E})$	$i \frac{g^2 m_t \hat{E}}{4m_W^2} (\delta_{h_{WW}} + \delta_{thh} + \mathcal{O}(\delta\kappa_{Z,\gamma}, \delta_{Z_{1L}}, \delta_{Z_{1R}}))$

the $(0, 0, \frac{1}{2}, -\frac{1}{2})$ configuration is due to the left-handed bottom quark exchange diagram in the $\phi^+ \phi^- \rightarrow t\bar{t}$ process. Note that if the bottom quark mass were not set to zero in our calculation, there would be a similar term with m_b^2/v^2 in the $(0, 0, -\frac{1}{2}, \frac{1}{2})$ configuration. Following this reasoning,

we can understand the processes involving only one longitudinal gauge boson $W^\pm \phi^\mp \rightarrow t\bar{t}$.

Secondly, we can see from the Table I that for the anomalous triple gauge boson couplings $\delta\kappa_{Z,\gamma}$ in the $(\mp \frac{1}{2}, \pm \frac{1}{2})$ top quark pair helicities and the anomalous

TABLE III. Energy scaling for cross sections and statistical signal significance of $W^+W^- \rightarrow t\bar{t}$ in different helicity categories with different anomalous couplings. The results for δ_{hWW} has the same behavior as δ_{tth} and therefore are not shown here. Note that we have highlighted the energy-growing behavior of the statistical signal significance in bold.

$(h_{W^+}, h_{W^-}, h_t, h_{\bar{t}})$	$\hat{\sigma}_{\text{SM}}$	$\hat{\sigma}_{\delta_{tth}}$	$\hat{\sigma}_{\lambda_{Z,\gamma}}$	$\hat{\sigma}_{\delta\kappa_{Z,\gamma}}$	$\hat{\sigma}_{\delta_{Wtb}}$	$\hat{\sigma}_{\delta_{Z_{1L}}}$	$\hat{\sigma}_{\delta_{Z_{1R}}}$	$\hat{\sigma}_{\delta g_1^Z}$	$\frac{S_{\delta_{tth}}}{\sqrt{B}}$	$\frac{S_{\lambda_{Z,\gamma}}}{\sqrt{B}}$	$\frac{S_{\delta\kappa_{Z,\gamma}}}{\sqrt{B}}$	$\frac{S_{\delta_{Wtb}}}{\sqrt{B}}$	$\frac{S_{\delta_{Z_{1L}}}}{\sqrt{B}}$	$\frac{S_{\delta_{Z_{1R}}}}{\sqrt{B}}$	$\frac{S_{\delta g_1^Z}}{\sqrt{B}}$
(0, 0, -, +)	$\frac{1}{\hat{E}^2}$	×	×	\hat{E}^0	\hat{E}^0	\hat{E}^0	×	×	×	×	\hat{E}	\hat{E}	\hat{E}	×	×
(0, 0, +, -)	$\frac{1}{\hat{E}^2}$	×	×	\hat{E}^0	×	×	\hat{E}^0	×	×	×	\hat{E}	×	×	\hat{E}	×
(0, 0, \mp , \mp)	$\frac{1}{\hat{E}^4}$	$\frac{1}{\hat{E}^2}$	×	$\frac{1}{\hat{E}^2}$	×	$\frac{1}{\hat{E}^2}$	$\frac{1}{\hat{E}^2}$	×	\hat{E}^0	×	\hat{E}^0	×	\hat{E}^0	\hat{E}^0	×
(0, +, +, +)(-, 0, -, -)	$\frac{1}{\hat{E}^2}$	×	$\frac{1}{\hat{E}^2}$	$\frac{1}{\hat{E}^2}$	$\frac{1}{\hat{E}^2}$	$\frac{1}{\hat{E}^2}$	$\frac{1}{\hat{E}^2}$	$\frac{1}{\hat{E}^2}$	×	$\frac{1}{\hat{E}}$	$\frac{1}{\hat{E}}$	$\frac{1}{\hat{E}}$	$\frac{1}{\hat{E}}$	$\frac{1}{\hat{E}}$	$\frac{1}{\hat{E}}$
(0, +, -, -)(-, 0, +, +)	$\frac{1}{\hat{E}^6}$	×	$\frac{1}{\hat{E}^4}$	$\frac{1}{\hat{E}^4}$	$\frac{1}{\hat{E}^4}$	$\frac{1}{\hat{E}^4}$	$\frac{1}{\hat{E}^4}$	$\frac{1}{\hat{E}^4}$	×	$\frac{1}{\hat{E}}$	$\frac{1}{\hat{E}}$	$\frac{1}{\hat{E}}$	$\frac{1}{\hat{E}}$	$\frac{1}{\hat{E}}$	$\frac{1}{\hat{E}}$
(+, 0, -, -)(0, -, -, -)	$\frac{1}{\hat{E}^6}$	×	$\frac{1}{\hat{E}^4}$	$\frac{1}{\hat{E}^4}$	$\frac{1}{\hat{E}^4}$	$\frac{1}{\hat{E}^4}$	$\frac{1}{\hat{E}^4}$	$\frac{1}{\hat{E}^4}$	×	$\frac{1}{\hat{E}}$	$\frac{1}{\hat{E}}$	$\frac{1}{\hat{E}}$	$\frac{1}{\hat{E}}$	$\frac{1}{\hat{E}}$	$\frac{1}{\hat{E}}$
(0, -, +, +)(+, 0, +, +)	$\frac{1}{\hat{E}^6}$	×	$\frac{1}{\hat{E}^4}$	$\frac{1}{\hat{E}^4}$	$\frac{1}{\hat{E}^4}$	$\frac{1}{\hat{E}^4}$	$\frac{1}{\hat{E}^4}$	$\frac{1}{\hat{E}^4}$	×	$\frac{1}{\hat{E}}$	$\frac{1}{\hat{E}}$	$\frac{1}{\hat{E}}$	$\frac{1}{\hat{E}}$	$\frac{1}{\hat{E}}$	$\frac{1}{\hat{E}}$
(+, 0, -, +)(0, -, -, +)	$\frac{1}{\hat{E}^4}$	×	$\frac{1}{\hat{E}^2}$	$\frac{1}{\hat{E}^2}$	$\frac{1}{\hat{E}^2}$	$\frac{1}{\hat{E}^2}$	×	$\frac{1}{\hat{E}^2}$	×	\hat{E}^0	\hat{E}^0	\hat{E}^0	\hat{E}^0	×	\hat{E}^0
(-, 0, -, +)(0, +, -, +)	$\frac{1}{\hat{E}^4}$	×	$\frac{1}{\hat{E}^2}$	$\frac{1}{\hat{E}^2}$	$\frac{1}{\hat{E}^2}$	$\frac{1}{\hat{E}^2}$	×	$\frac{1}{\hat{E}^2}$	×	\hat{E}^0	\hat{E}^0	\hat{E}^0	\hat{E}^0	×	\hat{E}^0
(+, 0, +, -)(0, -, +, -)	$\frac{1}{\hat{E}^4}$	×	$\frac{1}{\hat{E}^2}$	$\frac{1}{\hat{E}^2}$	×	×	$\frac{1}{\hat{E}^2}$	$\frac{1}{\hat{E}^2}$	×	\hat{E}^0	\hat{E}^0	×	×	\hat{E}^0	\hat{E}^0
(-, 0, +, -)(0, +, +, -)	$\frac{1}{\hat{E}^4}$	×	$\frac{1}{\hat{E}^2}$	$\frac{1}{\hat{E}^2}$	×	×	$\frac{1}{\hat{E}^2}$	$\frac{1}{\hat{E}^2}$	×	\hat{E}^0	\hat{E}^0	×	×	\hat{E}^0	\hat{E}^0
(\pm , \mp , -, +)	$\frac{1}{\hat{E}^2}$	×	×	×	$\frac{1}{\hat{E}^2}$	×	×	×	×	×	×	$\frac{1}{\hat{E}}$	×	×	×
(+, +, -, -)	$\frac{1}{\hat{E}^8}$	×	$\frac{1}{\hat{E}^4}$	×	×	×	×	×	×	\hat{E}^0	×	×	×	×	×
(-, -, -, -)	$\frac{1}{\hat{E}^4}$	×	$\frac{1}{\hat{E}^2}$	×	×	×	×	×	×	\hat{E}^0	×	×	×	×	×
(\pm , \mp , -, -)	$\frac{1}{\hat{E}^4}$	×	×	×	$\frac{1}{\hat{E}^4}$	×	×	×	×	×	×	$\frac{1}{\hat{E}^2}$	×	×	×
(\pm , \mp , +, +)	$\frac{1}{\hat{E}^4}$	×	×	×	$\frac{1}{\hat{E}^4}$	×	×	×	×	×	×	$\frac{1}{\hat{E}^2}$	×	×	×
(+, +, +, +)	$\frac{1}{\hat{E}^4}$	×	$\frac{1}{\hat{E}^2}$	×	×	×	×	×	×	\hat{E}^0	×	×	×	×	×
(-, -, +, +)	$\frac{1}{\hat{E}^8}$	×	$\frac{1}{\hat{E}^4}$	×	×	×	×	×	×	\hat{E}^0	×	×	×	×	×
(\pm , \pm , -, +)	$\frac{1}{\hat{E}^6}$	×	$\frac{1}{\hat{E}^2}$	×	×	×	×	×	×	\hat{E}	×	×	×	×	×
(\pm , \pm , +, -)	$\frac{1}{\hat{E}^6}$	×	$\frac{1}{\hat{E}^2}$	×	×	×	×	×	×	\hat{E}	×	×	×	×	×

top quark electroweak coupling $\delta_{Wtb}, \delta_{Z_{1L}}(\delta_{Z_{1R}})$ in the $(-\frac{1}{2}, \frac{1}{2})$ $(\frac{1}{2}, -\frac{1}{2})$ top quark pair helicities, the helicity amplitudes from longitudinal gauge bosons scale like \hat{E}^2 , while the SM contributions stay constant in the high energy limit. As discussed above, this means that for both the exclusive channel with all the helicities of the particles fully measured and the inclusive channel where all the helicity configurations are included, the statistical significance scales like \hat{E} , which results in larger sensitivity for higher energy bins. However, for the modification of the top Yukawa coupling δ_{tth} in the high energy limit,³ the helicity amplitude only grows linearly as \hat{E} in the $(0, 0, \mp\frac{1}{2}, \mp\frac{1}{2})$ helicity configuration, and the SM contribution decreases like $1/\hat{E}$. This in turn leads to the constant behavior for the statistical significance in the exclusive channel and decreasing statistical significance as $\mathcal{O}(1/\hat{E})$ in the inclusive channel. This means that in the realistic case at the muon collider, the sensitivity on the top Yukawa coupling from the electroweak top pair production would

mostly come from low energy bins. The high energy muon collider benefits us from the growth of the VBF cross sections, i.e., the enhancement of the vector boson parton luminosity. We finally note that for the case of systematical uncertainty dominance, the significance grows as energy increases for all anomalous couplings in the exclusive channel. For the fully inclusive channel, the significance grows as \hat{E}^2 for the anomalous couplings $\delta\kappa_{Z,\gamma}, \delta_{Wtb}, \delta_{Z_{1L}}, \delta_{Z_{1R}}$, but stays constant for aTGC $\lambda_{Z,\gamma}$ and the anomalous top Yukawa coupling δ_{tth} .

Now we examine the threshold behavior of top quark electroweak pair production. We expand the helicity amplitudes in terms of the top quark velocity β_t around the $\sqrt{s} \sim 2m_t$. For simplicity, we also keep only the leading power of $m_{W,Z}^2/m_t^2$. The results are presented in Table IV for the helicity configurations $(h_t, h_{\bar{t}}) = (\mp\frac{1}{2}, \pm\frac{1}{2})$ and listed in Table V for the helicity configurations $(h_t, h_{\bar{t}}) = (\mp\frac{1}{2}, \mp\frac{1}{2})$. We can see from the tables that all the SM helicity amplitudes arise at the zeroth order of top quark velocity β_t^0 except the helicity configurations for $(h_{W^+}, h_{W^-}) = (\pm 1, \mp 1)$ as they arise from the $J \geq 2$ partial waves. We also find that for the processes involving the longitudinal W bosons, there is an additional factor of

³Likewise for the anomalous Higgs gauge boson coupling δ_{hWW} , as only the combination of $\delta_{tth} + \delta_{hWW}$ appears in the helicity amplitudes at linear order.

TABLE IV. Threshold behaviors of the helicity amplitude for $W^+W^- \rightarrow t\bar{t}$ with $h_t - h_{\bar{t}} = \mp 1$. Here we keep the leading terms in the top velocity β_t expansion and $\frac{m_{W,Z}^2}{m_t^2}$ expansion.

$(h_t, h_{\bar{t}})$	(h_{W^+}, h_{W^-})	$\tilde{\mathcal{M}}_{h_{W^+}h_{W^-};h_t,h_{\bar{t}}}^{\text{SM}}$	$\tilde{\mathcal{M}}_{h_{W^+}h_{W^-};h_t,h_{\bar{t}}}^{\text{BSM}}$
$(\mp \frac{1}{2} \pm \frac{1}{2})$	$(+1 -1), (-1 +1)$	$\mathcal{O}(\beta_t)$	$\mathcal{O}(\beta_t \delta_{Wtb})$
	$(+1 +1), (-1 -1)$	$-i \frac{g^2}{2\sqrt{2}}$	$i \frac{g^2(3\lambda_Z + 8s_W^2(\lambda_\gamma - \lambda_Z))m_t^2}{3\sqrt{2}m_W^2}$
	$(+1 0), (0 -1)$	$-i \frac{g^2 m_t}{\sqrt{2}m_W}$	$\mathcal{O}\left(\frac{m_t}{m_W}(\delta_{Wtb}, \lambda_{Z,\gamma}, \delta g_1^Z, \delta \kappa_{Z,\gamma}, \delta_{Z_{1L}}, \delta_{Z_{1R}})\right)$
	$(-1 0), (0 +1)$	$-i \frac{g^2 m_t}{\sqrt{2}m_W}$	$\mathcal{O}\left(\frac{m_t}{m_W}(\lambda_{Z,\gamma}, \delta g_1^Z, \delta \kappa_{Z,\gamma}, \delta_{Z_{1L}}, \delta_{Z_{1R}})\right)$
	$(0 0)$	$-i \frac{g^2 m_t^2}{\sqrt{2}m_W^2}$	$i \frac{g^2(-3(\delta \kappa_Z + \delta_{Z_{1L}}) + 4s_W^2(2\delta \kappa_Z - 2\delta \kappa_\gamma + \delta_{Z_{1L}} + \delta_{Z_{1R}}))m_t^2}{3\sqrt{2}m_W^2}$

TABLE V. Threshold behaviors of the helicity amplitude for $W^+W^- \rightarrow t\bar{t}$ with $h_t - h_{\bar{t}} = 0$. Here we keep the leading terms in the top velocity β_t expansion and $\frac{m_{W,Z}^2}{m_t^2}$ expansion.

$(h_t, h_{\bar{t}})$	(h_{W^+}, h_{W^-})	$\tilde{\mathcal{M}}_{h_{W^+}h_{W^-};h_t,h_{\bar{t}}}^{\text{SM}}$	$\tilde{\mathcal{M}}_{h_{W^+}h_{W^-};h_t,h_{\bar{t}}}^{\text{BSM}}$
$(-\frac{1}{2} - \frac{1}{2})$	$(+1 -1), (-1 +1)$	$\mathcal{O}(\beta_t)$	$\mathcal{O}(\beta_t \delta_{Wtb})$
	$(+1 +1), (-1, -1)$	$ig^2 \frac{\pm 2 - \cos \theta}{4}$	$i \frac{g^2(3\lambda_Z + 8s_W^2(\lambda_\gamma - \lambda_Z))m_t^2 \cos \theta}{6m_W^2}$
	$(+1 0), (0 -1)$	$-ig^2 \frac{m_t}{2m_W}$	$\mathcal{O}\left(\frac{m_t}{m_W}(\delta_{Wtb}, \lambda_{Z,\gamma}, \delta g_1^Z, \delta \kappa_{Z,\gamma}, \delta_{Z_{1L}}, \delta_{Z_{1R}})\right)$
	$(-1 0), (0, +1)$	$-ig^2 \frac{m_t}{2m_W}$	$\mathcal{O}\left(\frac{m_t}{m_W}(\lambda_{Z,\gamma}, \delta g_1^Z, \delta \kappa_{Z,\gamma}, \delta_{Z_{1L}}, \delta_{Z_{1R}})\right)$
	$(0 0)$	$-i \frac{g^2 m_t^2}{2m_W^2} \cos \theta$	$i \frac{g^2(-3\delta(\kappa_Z + \delta_{Z_{1L}}) + 4s_W^2(2\delta \kappa_Z - 2\delta \kappa_\gamma + \delta_{Z_{1L}} + \delta_{Z_{1R}}))m_t^2 \cos \theta}{6m_W^2} + i \frac{2g^2 m_t^4 \beta_t (\delta_{th} + \delta_{hWW})}{(m_h^2 - 4m_t^2)m_W^2}$
$(\frac{1}{2} \frac{1}{2})$	$(+1 -1), (-1 +1)$	$\mathcal{O}(\beta_t)$	$\mathcal{O}(\beta_t \delta_{Wtb})$
	$(+1 +1), (-1, -1)$	$ig^2 \frac{\pm 2 + \cos \theta}{4}$	$-i \frac{g^2(3\lambda_Z + 8s_W^2(\lambda_\gamma - \lambda_Z))m_t^2 \cos \theta}{6m_W^2}$
	$(+1 0), (0 -1)$	$ig^2 \frac{m_t}{2m_W}$	$\mathcal{O}\left(\frac{m_t}{m_W}(\delta_{Wtb}, \lambda_{Z,\gamma}, \delta g_1^Z, \delta \kappa_{Z,\gamma}, \delta_{Z_{1L}}, \delta_{Z_{1R}})\right)$
	$(-1 0), (0, +1)$	$ig^2 \frac{m_t}{2m_W}$	$\mathcal{O}\left(\frac{m_t}{m_W}(\lambda_{Z,\gamma}, \delta g_1^Z, \delta \kappa_{Z,\gamma}, \delta_{Z_{1L}}, \delta_{Z_{1R}})\right)$
	$(0 0)$	$i \frac{g^2 m_t^2}{2m_W^2} \cos \theta$	$-i \frac{g^2(-3\delta(\kappa_Z + \delta_{Z_{1L}}) + 4s_W^2(2\delta \kappa_Z - 2\delta \kappa_\gamma + \delta_{Z_{1L}} + \delta_{Z_{1R}}))m_t^2 \cos \theta}{6m_W^2} - i \frac{2g^2 m_t^4 \beta_t (\delta_{th} + \delta_{hWW})}{(m_h^2 - 4m_t^2)m_W^2}$

m_t/m_W enhancement for each longitudinal mode. For the anomalous TGCs $\delta \kappa_{Z,\gamma}$ in the helicity configuration of the longitudinal W^\pm bosons and $\lambda_{Z,\gamma}$ in the helicity configurations $(h_{W^+}, h_{W^-}) = (\pm 1, \pm 1)$, the amplitudes at threshold are enhanced by m_t^2/m_W^2 for all the helicity configurations of top quark pair. Since the SM contribution to amplitudes of $(h_{W^+}, h_{W^-}) = (\pm 1, \pm 1)$ at threshold are not suppressed, it provides an interesting possibility to measure aTGCs $\lambda_{Z,\gamma}$, which we leave for future studies. For the top Yukawa coupling modification δ_{th} , its leading contribution to the longitudinal W^\pm gauge boson arises at order β_t , which means that the linear BSM helicity cross sections arise at β_t^2 .⁴ The statistical significance will scale

like β_t^3 in the small β_t approximation, and we need to have sizable top quark velocity to achieve maximal sensitivity.

We finally comment on the scattering angle θ distribution, where θ is the polar angle between the outgoing top quark and incoming W^+ boson. As is well known, there is a t -channel singularity in the cross section of this process, which can be seen from the high energy limit in Table I and appears in the helicity configuration $(h_{W^+}, h_{W^-}, h_t, h_{\bar{t}}) = (-1, +1, -\frac{1}{2}, \frac{1}{2})$. Note that to obtain the θ distribution for the helicity amplitudes, one needs to bring back the Wigner d functions. For the t -channel singularity, the relevant functions are as follows:

$$d_{-2,-1}^2 = \frac{1}{2} \sin \theta (1 + \cos \theta),$$

$$d_{2,-1}^2 = -\frac{1}{2} \sin \theta (1 - \cos \theta). \quad (11)$$

⁴The extra β_t comes in because the final two-body phase space has linear dependence on the velocity of the top quark.

We can see that for other helicity configuration $(h_{W^+}, h_{W^-}, h_t, h_{\bar{t}}) = (+1, -1, -\frac{1}{2}, \frac{1}{2})$, the t -channel pole is canceled by the kinematical zero in the Wigner function $d_{2,-1}^2(\theta)$. The differential helicity cross section with respect to $\cos\theta$ for the t -channel singularity in the high energy limit scales like

$$\frac{d\sigma^{(h_{W^+}, h_{W^-})=(+1, -1)}}{d\cos\theta} \sim \frac{\sin^2\theta(1+\cos\theta)^2}{(1-\cos\theta)^2} \sim \frac{(1+\cos\theta)^3}{1-\cos\theta}, \quad (12)$$

which strongly peaks in the forward region with an enhanced factor of $s/4m_t^2$. On the other hand, the anomalous top Yukawa coupling δ_{tth} appears in the longitudinal gauge boson helicity configuration, and the differential cross section in the high energy limit reads as

$$\frac{d\sigma^{(h_{W^+}, h_{W^-})=(0,0)}}{d\cos\theta} \sim \sin^2\theta, \quad (13)$$

which has its maximum near the central region $\theta \sim \pi/2$. This means that at the high energy bin, the sensitivity on the top Yukawa coupling measurement will mostly come from the central region where the transverse W -parton distribution functions (PDFs) are suppressed.

At the threshold, the top quark pair production from the longitudinal gauge boson fusion is enhanced by a factor of m_t^4/m_W^4 . By focusing on this helicity category, the statistical significance for the top Yukawa coupling behaves as

$$\frac{S}{\sqrt{B}} \sim \sin\theta \cos\theta, \quad (14)$$

where for the SM background, we only include the helicity conserving top quark pair production, i.e., $(h_t, h_{\bar{t}}) = (\mp\frac{1}{2}, \pm\frac{1}{2})$, which is a factor of 2 larger than the helicity violating ones. The significance peaks around $\theta \sim \pi/4$.

C. Weak boson PDF and energy scaling behavior

In this section, we analyze the energy scaling behavior of $\mu^+\mu^- \rightarrow X\bar{X}\nu\bar{\nu}$ processes by making use of the effective W -boson approximation. As illustrated in Fig. 2, EWA states that at sufficiently high energies and suitable kinematical regimes (hard scattering limit), the cross section for the process $\mu^+\mu^- \rightarrow X\bar{X}\nu\bar{\nu}$ can be factorized into the on shell hard subprocess $V\bar{V} \rightarrow X\bar{X}$ convoluted with the W -boson parton distribution functions

$$\begin{aligned} \sigma(\mu^+\mu^- \rightarrow X\bar{X}\nu\bar{\nu})(s) &= \int_{\tau_0}^1 d\tau \sum_{ij} \Phi_{ij}(\tau, \mu_f) \\ &\times \hat{\sigma}(ij \rightarrow X\bar{X})(\tau s), \end{aligned} \quad (15)$$

where \sqrt{s} is the center-of-mass energy of muons and $\sqrt{\hat{s}} = \sqrt{\tau s}$ is the center-of-mass energy of the $X\bar{X}$. Here

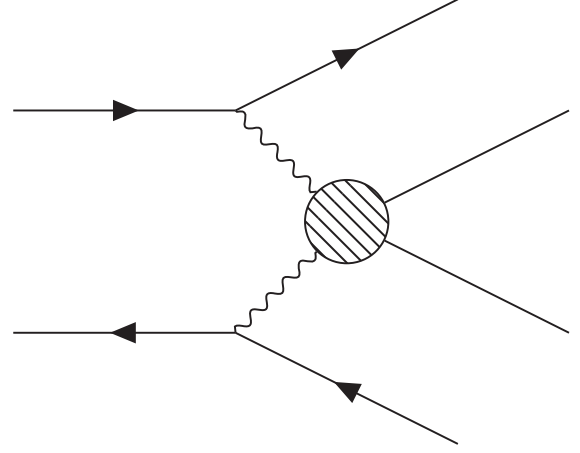


FIG. 2. Illustration of the EWA approximation at the muon collider.

$V = W^\pm, Z$ denotes any of the SM massive electroweak gauge bosons.⁵ The parton luminosity $\Phi_{ij}(\tau, \mu_f)$ is given by [12]

$$\Phi_{ij}(\tau, \mu_f) = \int_{\tau}^1 \frac{d\xi}{\xi} f_i(\xi, \mu_f) f_j\left(\frac{\tau}{\xi}, \mu_f\right). \quad (16)$$

Here μ_f is the factorization scale in the process under study, and the weak boson PDFs at muon collider read as

$$\begin{aligned} f_{\mu^+/\nu_\lambda}(\xi, \mu_f, \lambda = \pm 1) &= \frac{C}{16\pi^2} \frac{(g_V^\mu \mp g_A^\mu)^2 + (g_V^\mu \pm g_A^\mu)^2(1-\xi)^2}{\xi} \log\left(\frac{\mu_f^2}{M_V^2}\right) \\ f_{\mu^+/\nu_\lambda}(\xi, \mu_f, \lambda = 0) &= \frac{C}{4\pi^2} ((g_V^\mu)^2 + (g_A^\mu)^2) \left(\frac{1-\xi}{\xi}\right). \end{aligned} \quad (17)$$

Note that for the gauge boson PDFs of the μ^- beam, we have the following relation [45]:

$$f_{\mu^-/\nu_\lambda}(\xi, \mu_f) = f_{\mu^+/\bar{\nu}_{-\lambda}}(\xi, \mu_f), \quad (18)$$

where \bar{V} is the charge conjugate of V and the electric charge of the V is determined by the charge conservation. The coupling constants C, g_V^μ, g_A^μ denote the corresponding muon-weak-boson couplings and for the W^\pm -boson, it reads as⁶

⁵We will not discuss the $\gamma\gamma$ PDF here.

⁶Note that in the presence of anomalous gauge-boson fermion $\delta_{Wtb}, \delta_{ZtL}, \delta_{ZtR}$, the W, Z gauge boson PDFs will also be changed. Since the changes are overall constants, it will not modify the energy scaling behavior of the anomalous couplings.

TABLE VI. Best fit for $\Phi_{W^+W^-}$ for different ranges of τ without including the log terms.

h_{W^+}	h_{W^-}	$10^{-4} \leq \tau \leq 0.01$	$0.01 \leq \tau \leq 0.2$	$0.2 \leq \tau \leq 0.8$	$0.8 \leq \tau \leq 0.95$
–	–	$\frac{1}{\tau^{1.2}}$	$\frac{1}{\tau^{1.4}}$	$\frac{1}{\tau^{2.9}}$	$\frac{1}{\tau^{1.8}}$
0	0	$\frac{1}{\tau^{1.2}}$	$\frac{1}{\tau^{1.5}}$	$\frac{1}{\tau^{3.0}}$	$\frac{1}{\tau^{1.8}}$
+	+	$\frac{1}{\tau^{1.2}}$	$\frac{1}{\tau^{1.4}}$	$\frac{1}{\tau^{2.9}}$	$\frac{1}{\tau^{1.8}}$
–	+	$\frac{1}{\tau^{1.2}}$	$\frac{1}{\tau^{1.7}}$	$\frac{1}{\tau^{3.9}}$	$\frac{1}{\tau^{2.7}}$
+	–	$\frac{1}{\tau^{1.1}}$	$\frac{1}{\tau^{1.3}}$	$\frac{1}{\tau^{2.1}}$	$\frac{1}{\tau^2}$
–	0	$\frac{1}{\tau^{1.2}}$	$\frac{1}{\tau^{1.5}}$	$\frac{1}{\tau^{3.4}}$	$\frac{1}{\tau^{2.2}}$
0	–	$\frac{1}{\tau^{1.1}}$	$\frac{1}{\tau^{1.4}}$	$\frac{1}{\tau^{2.5}}$	$\frac{1}{\tau^{1.3}}$
+	0	$\frac{1}{\tau^{1.1}}$	$\frac{1}{\tau^{1.4}}$	$\frac{1}{\tau^{2.5}}$	$\frac{1}{\tau^{1.3}}$
0	+	$\frac{1}{\tau^{1.2}}$	$\frac{1}{\tau^{1.5}}$	$\frac{1}{\tau^{3.4}}$	$\frac{1}{\tau^{2.2}}$

$$C = \frac{g^2}{8}, \quad g_V^\mu = -g_A^\mu = 1, \quad (19)$$

while for the Z boson, we have

$$C = \frac{g^2}{\cos^2 \theta_W}, \quad g_V^\mu = \frac{1}{2}(T_L^3)^\mu + \sin^2 \theta_W,$$

$$g_A = -\frac{1}{2}(T_L^3)^\mu, \quad (20)$$

where we have neglected the masses of the muons. Note that $(T_L^3)^{\mu_L} = -\frac{1}{2}$, $(T_L^3)^{\mu_R} = 0$. We will focus on the W^+W^- parton luminosity, since it is dominant compared with ZZ . To obtain the energy scaling behavior of the parton luminosity $\Phi_{W^+W^-}$, we first divide the allowed values of the parameter τ into four regions, $[10^{-4}, 0.01]$, $[0.01, 0.2]$, $[0.2, 0.8]$, $[0.8, 0.95]$, and then approximate the dependence of $\Phi_{W^+W^-}$ on τ as τ^{-n} in each region. The results are shown in Table VI, where we neglected the scale-dependent logarithmic terms.⁷ Recalling the relations $\tau = \frac{\hat{s}}{s}$ and $\sqrt{\hat{s}} = \hat{E}$, the dependence on τ can be translated into the dependence on the invariant mass of W^+W^- system \hat{E}^{-2n} for constant invariant mass of the $\mu^+\mu^-$ system. We can see that due to the absence of the $(1 - \xi)^2$ term in Eq. (17) for the plus helicity of the W boson, the parton luminosity $\Phi_{W^+W^-}(\tau)$ in the $(h_{W^+}, h_{W^-}) = (+, +)$ category has the mildest decrease as τ increases.

Then from Eq. (15), we can see that the differential cross section in the invariant mass of $X\bar{X}$ becomes

$$\frac{d\sigma}{d\hat{E}}(\mu^+\mu^- \rightarrow X\bar{X}\nu\bar{\nu}) = \frac{2\hat{E}}{s} \sum_{h_2, h_2} \Phi_{W_{h_1}^+ W_{h_2}^-}(\hat{E})$$

$$\times \hat{\sigma}(W_{h_1}^+ W_{h_2}^- \rightarrow X\bar{X}). \quad (21)$$

Now for the most ideal scenario where the helicities of the initial and final particles can be measured and assuming

⁷We have checked that the results will not be changed significantly by including the log terms.

that statistical error is dominant, the signal significance scales like

$$\frac{S}{\sqrt{B}} \sim \frac{\frac{d\sigma_S}{d\hat{E}}}{\sqrt{\frac{d\sigma_B}{d\hat{E}}}} \sim \sqrt{\frac{\Phi_{W_{h_1}^+ W_{h_2}^-}}{\hat{E}} \mathcal{M}_{\delta_i}^{h_1 h_2 h_3 h_4}}{\hat{E}^{n+\frac{1}{2}}}} \sim \frac{\mathcal{M}_{\delta_i}^{h_1 h_2 h_3 h_4}}{\hat{E}^{n+\frac{1}{2}}}, \quad (22)$$

where we have used the energy scaling of the parton luminosity $\Phi_{W^+W^-} \sim \hat{E}^{-2n}$ and keep the center-of-mass energy of the muons \sqrt{s} as constant. From Table VI, we can see that the statistical significance decreases for the linear energy growth of BSM helicity amplitude in the whole considered regions and increases or stays constant for the quadratic energy growth for $\tau \in [10^{-4}, 0.2]$. For higher τ values ($\tau \gtrsim 0.2$), the statistical significance decreases at least as \hat{E}^{-1} for the quadratic energy growth of the BSM helicity amplitude. A similar conclusion holds for the fully inclusive case if we replace $\mathcal{M}_{\delta_i}^{h_1 \dots h_4}$ with $\mathcal{M}_{\delta_i}^{h_1 \dots h_4} \mathcal{M}_{SM}^{h_1 \dots h_4}$, as can be seen from the energy scaling of the statistical signal significance as follows:

$$\frac{S}{\sqrt{B}} \sim \frac{\frac{d\sigma_S}{d\hat{E}}}{\sqrt{\frac{d\sigma_B}{d\hat{E}}}} \sim \frac{1}{\sqrt{\hat{E}}} \frac{\sum_{h_1 \dots h_4} \Phi_{W_{h_1}^+ W_{h_2}^-} \mathcal{M}_{SM}^{h_1 \dots h_4} \mathcal{M}_{\delta_i}^{h_1 \dots h_4}}{\sqrt{\sum_{h_1 \dots h_4} \Phi_{W_{h_1}^+ W_{h_2}^-} (\mathcal{M}_{SM}^{h_1 \dots h_4})^2}}. \quad (23)$$

By using the energy scaling behavior of parton luminosity $\Phi_{W^+W^-}$ in Table VI and partonic cross section in Table III for the process $\mu^+\mu^- \rightarrow i\bar{i}\nu\bar{\nu}$ in the presence of anomalous couplings, we can obtain the energy scaling for the statistical signal significance in the fully inclusive case. For the top Yukawa coupling δ_{tth} and the Higgs gauge boson coupling δ_{hWW} , the result reads as

$$\frac{S}{\sqrt{B}} \sim \hat{E}^{-1.8}, \hat{E}^{-2.1}, \hat{E}^{-4}, \quad \text{for}$$

$$\tau \in [10^{-4}, 0.01], [0.01, 0.2], [0.2, 0.8], \quad (24)$$

where we have omitted the highest τ region. As expected, the sensitivity on the top Yukawa coupling decreases as bin

energy becomes larger. For the anomalous coupling $\delta\kappa_{Z,\gamma}, \delta\kappa_{Wtb}, \delta\kappa_{Zt_L}, \delta\kappa_{Zt_R}$, the sensitivity scales like

$$\frac{S}{\sqrt{B}} \sim \hat{E}^{0.2}, \hat{E}^{-0.1}, \hat{E}^{-2}, \quad \text{for} \\ \tau \in [10^{-4}, 0.01], [0.01, 0.2], [0.2, 0.8], \quad (25)$$

from which, we can see that there is a mild increase for the signal significance at low τ , a mild decrease for the intermediate τ , and a decrease at high τ . Finally, we find that for the anomalous coupling $\lambda_{Z,\gamma}$, the energy scaling behaves as

$$\frac{S}{\sqrt{B}} \sim \hat{E}^{-1.6}, \hat{E}^{-1.7}, \hat{E}^{-2.2}, \quad \text{for} \\ \tau \in [10^{-4}, 0.01], [0.01, 0.2], [0.2, 0.8], \quad (26)$$

and for the coupling δg_1^Z , we have

$$\frac{S}{\sqrt{B}} \sim \hat{E}^{-1.6}, \hat{E}^{-1.9}, \hat{E}^{-3}, \quad \text{for} \\ \tau \in [10^{-4}, 0.01], [0.01, 0.2], [0.2, 0.8], \quad (27)$$

which decreases with the energy bins.

III. TOP YUKAWA COUPLINGS AT THE HIGH ENERGY MUON COLLIDER

In this section, we study in detail the prospects of measuring the top Yukawa coupling at a high energy muon collider. To quantify the importance of the anomalous couplings, we parametrize the cross sections as

$$\sigma = \sigma_{\text{SM}}(1 + R_1\delta + R_2\delta^2), \quad (28)$$

where δ_i signifies some fractional deviation in a SM coupling. Throughout this paper, we will be primarily considering the interference term which is linear in δ , but we also remark on the inclusion of the quadratic term. In terms of the kappa framework [51], δ_i and κ_i are related by $\kappa_i = 1 + \delta_i$.

Before we present the detailed analysis for the VBF production of the top quark pair, we make some comments about the Drell-Yan processes which are also involving top Yukawa coupling. The relevant processes are

$$\mu^+\mu^- \rightarrow t\bar{t}, t\bar{t}h, \quad (29)$$

in which there is no energy growing behavior for the anomalous top Yukawa coupling δ_{tth} . In Fig. 3, we have plotted the SM cross sections as functions of center-of-mass energy of the muon collider for both Drell-Yan (DY) and VBF productions of the top quark pair and top quark

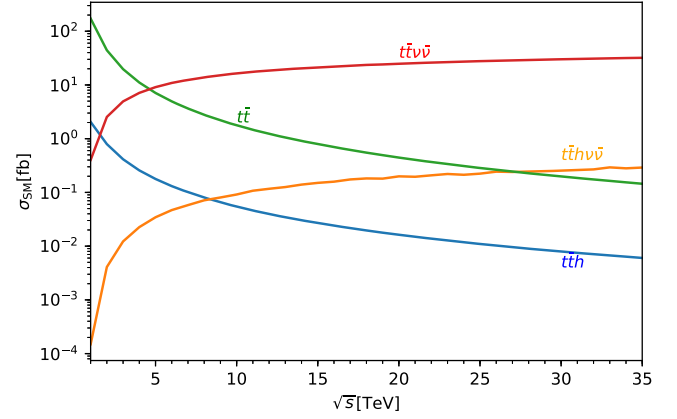


FIG. 3. Cross section of SM $\mu^+\mu^- \rightarrow t\bar{t}$, $\mu^+\mu^- \rightarrow t\bar{t}h$, and $\mu^+\mu^- \rightarrow t\bar{t}\nu\bar{\nu}$ with the on shell Z contribution removed.

pair plus a Higgs boson. We can see that due to the logarithmic growth of the VBF processes and the inverse of energy squared decrease of the DY processes, the VBF productions start to become dominant at 5 (8) TeV center-of-mass energy for the $t\bar{t}$ ($t\bar{t}h$). Besides the small cross sections at the high energy muon collider, the R values defined in Eq. (28) are also very small for the DY production of the top quark pair. In order to have the $t\bar{t}$ process involve the top Yukawa coupling, it is necessary to include the nonzero muon masses. In this case, the dependence of the cross section on δ_{tth} will be suppressed by the muon Yukawa coupling squared $m_\mu^2/v^2 \sim 2 \times 10^{-7}$. We have checked that for this process, the R ratios defined in Eq. (28) for the anomalous coupling δ_{tth} are very small:

$$R_1 = 2.337 \times 10^{-5}, \quad R_2 = 1.169 \times 10^{-5} \quad @10 \text{ TeV} \\ R_1 = 2.343 \times 10^{-5}, \quad R_2 = 1.172 \times 10^{-5} \quad @30 \text{ TeV}, \quad (30)$$

and we will not consider it any further. For the DY process $\mu^+\mu^- \rightarrow t\bar{t}h$, the R values are

$$R_1 = 1.62, \quad R_2 = 0.797 \quad @10 \text{ TeV} \\ R_1 = 1.56, \quad R_2 = 0.774 \quad @30 \text{ TeV}. \quad (31)$$

We can see that the R values stay almost constant as the center-of-mass energy of the muon collider increases. We expect that the sensitivity on the top Yukawa coupling from this process will come from the lower energy stages of the muon collider. Such analysis has been performed at CLIC in the baseline energy of 1.4 TeV [52].

A. Simulation and cuts

We now turn to the simulation and analysis of the process $\mu^+\mu^- \rightarrow t\bar{t}\nu_\mu\bar{\nu}_\mu, t\bar{t}h\nu_\mu\bar{\nu}_\mu$ in the presence of the anomalous

TABLE VII. Comparison between EWA and full LO matrix element calculations (LOME) at MadGraph5 for the cross sections of $\mu^+\mu^- \rightarrow t\bar{t}\nu_\mu\bar{\nu}_\mu$ and $\mu^+\mu^- \rightarrow t\bar{t}h\nu_\mu\bar{\nu}_\mu$. For the LOME calculation, the cut on the recoil mass in Eq. (34) has been imposed.

\sqrt{s} (TeV) \ σ_{SM} (fb)	6	10	14	30
$t\bar{t}\nu_\mu\bar{\nu}_\mu$				
LOME	11.4	17.1	21.5	31.2
EWA	18.2	27.0	33.2	48.4
LOME $p_{T,t/\bar{t}} > 500$ GeV	0.27	0.63	0.95	1.9
EWA $p_{T,t/\bar{t}} > 500$ GeV	0.36	0.78	1.1	2.2
$t\bar{t}h\nu_\mu\bar{\nu}_\mu$				
LOME	0.049	0.094	0.14	0.26
EWA	0.075	0.15	0.23	0.48
LOME $p_{T,t/\bar{t}/h} > 500$ GeV	3.0×10^{-4}	1.3×10^{-3}	2.7×10^{-3}	8.4×10^{-3}
EWA $p_{T,t/\bar{t}/h} > 500$ GeV	3.3×10^{-4}	1.3×10^{-3}	2.5×10^{-3}	7.6×10^{-3}

top Yukawa coupling δ_{tth} . Note that EWA works well when the hard scattering scale is much larger than the masses of the massive gauge bosons, while in our case, we expect the sensitivity on the top Yukawa coupling comes from the near-threshold region. In this case, we will use MadGraph5 [53] leading order (LO) full matrix elements to calculate the cross sections and generate the events at LO for the kinematical distributions. In Table VII, we have shown the cross sections for the two processes in the SM case for both the EWA and full LO matrix element calculations without any cuts on the p_T of the tops, Higgs boson, and with p_T cut larger than 500 GeV. We can see that while EWA calculations usually lead to larger values for the cross section without the p_T cut, they tend to agree very well with LO matrix element results at hard scattering scale $p_T > 500$ GeV. See Refs. [14,54] for a thorough study of the EWA at the high energy muon collider. The anomalous coupling δ_{tth} is implemented by using the BSMC model file [55]. We will work at the level of top quarks, and no decaying of the top quarks will be simulated.

One advantage of the lepton colliders compared with the hadron collider is that the initial energies of the colliding leptons are known very precisely [1]; as a result, the invariant mass of the two outgoing neutrinos is indirectly determined by the momenta of the top quark pair or the top quark pair plus Higgs boson. This is defined as recoil mass, and for the $t\bar{t}\nu_\mu\bar{\nu}_\mu$ process,

$$M_{\text{recoil}}^2 = (p_{\mu^+} + p_{\mu^-} - p_t - p_{\bar{t}})^2. \quad (32)$$

For the $t\bar{t}h\nu_\mu\bar{\nu}_\mu$ process, it is given by

$$M_{\text{recoil}}^2 = (p_{\mu^+} + p_{\mu^-} - p_t - p_{\bar{t}} - p_h)^2. \quad (33)$$

We will impose the following cut on the recoil mass at the generator level:

$$M_{\text{recoil}} > 200 \text{ GeV}, \quad (34)$$

TABLE VIII. Cross sections for signal and background. For the VBF processes, the cut on the recoil mass in Eq. (34) has been imposed.

\sqrt{s} (TeV) \ σ_{SM} (fb)	3	6	10	14	30
$t\bar{t}\nu_\mu\bar{\nu}_\mu$	4.93	10.9	16.4	20.5	30.1
$t\bar{t}h\nu_\mu\bar{\nu}_\mu$	0.0121	0.0460	0.0914	0.141	0.269
$t\bar{t}$	19.7	4.95	1.78	0.909	0.198
$t\bar{t}h$	0.414	0.131	0.0547	0.0305	0.00793
$W^+W^-\nu_\mu\bar{\nu}_\mu^a$	120	259	399	515	815
$W^\pm Z\mu^\mp(\bar{\nu}_\mu/\nu_\mu)^b$	96.6	215	340	443	717

^aNote that there are also similar contributions from $ZZ/\gamma\gamma/Z\gamma$ fusion processes. As discussed below, we only assume some signal efficiency such that all the reducible SM backgrounds can be reduced to a negligible level.

^bSum of the cross sections for $W^+Z\mu^-\bar{\nu}$ and $W^-Z\mu^+\nu$ with $p_T > 30$ GeV for charged leptons and the on shell $W \rightarrow \mu\nu$ contribution removed.

which will remove the contribution from the process $t\bar{t}Z \rightarrow t\bar{t}(\nu\bar{\nu})$. In Table VIII, we have presented the cross sections of the VBF $t\bar{t}$ production and the potential relevant backgrounds for some benchmark scenarios at the high energy muon collider. For all the VBF processes, the cross sections are presented after the cut in Eq. (34).

The decaying branching ratios for the top quark pair are respectively 45%, 28%, 4.4% in the fully hadronically decaying channel, semileptonically decaying channel, and fully leptonically decaying channel [56,57].⁸ We will focus on the semileptonically decaying channel where the top quark and antitop quark can be reconstructed and distinguished by the charges of the decayed leptons.⁹ To suppress the beam induced background, we put the following cuts on

⁸In the estimation of the decaying branching ratios, we have neglected the $\tau\nu$ decay of the W bosons. Including it will have mild effects on the final results.

⁹See Ref. [58] for the study in both fully hadronic and semileptonic channels.

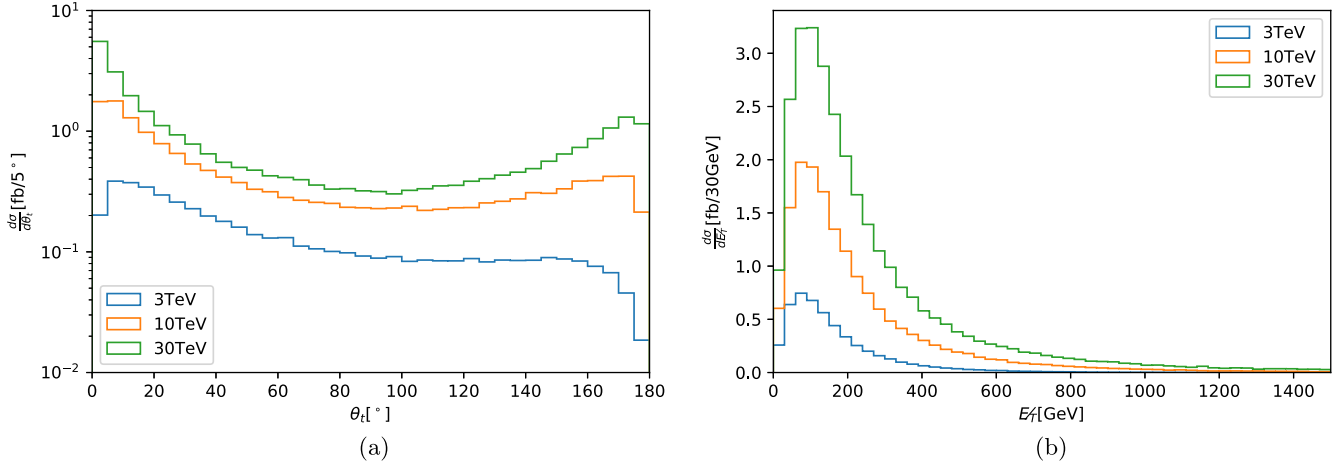


FIG. 4. Standard Model distribution of θ and p_T of the top quark at 3, 10, and 30 TeV muon colliders after the cut on the recoil mass in Eq. (34). (a) Standard Model θ_i . (b) Standard Model \cancel{E}_T of the top.

the polar angles of the top quark pair in the laboratory frame:

$$10^\circ < \theta_{i,\bar{i}} < 170^\circ, \quad (35)$$

where in our convention, the z axis aligns with the direction of the μ^+ beam. As shown in Fig. 4, the θ_i distribution peaks strongly in the forward region at 3, 10, 30 TeV muon collider and peaks also mildly in the backward region for 10, 30 TeV center-of-mass energy. The cut efficiencies for the $\theta_{i,\bar{i}}$ cuts at the 10 TeV and 30 TeV muon collider are 0.57 and 0.43, respectively. This reduces the cross sections of the SM $t\bar{t}v\bar{v}$ in the semileptonically decaying channel to 2.63 fb and 3.61 fb for 10 TeV and 30 TeV muon collider respectively. Here the numbers have also taken into account the branching ratios of the semileptonically decaying channel of top quark pair.

We expect that the signal manifests itself in the kinematical region where effective W approximation applies as this is the hard scattering regime. To maximize the sensitivity and also to help to reconstruct the effective W boson partonic center-of-mass frame, we impose the following criterion:

$$\cancel{E}_T < 200 \text{ GeV}, \quad (36)$$

where at the truth level, the missing transverse energy \cancel{E}_T is equal to the magnitude of the transverse momentum of the two neutrino system or top quark pair system:

$$\cancel{E}_T = |\vec{p}_{T,\nu} + \vec{p}_{T,\bar{\nu}}| = |\vec{p}_{T,t} + \vec{p}_{T,\bar{t}}|. \quad (37)$$

Note that we also require the missing transverse energy to be larger than 20 GeV:

$$\cancel{E}_T > 20 \text{ GeV}, \quad (38)$$

which is used to reduce the background from DY production of $t\bar{t}$ with initial state radiation or bremsstrahlung effects [52]. The cut efficiencies we obtain from comparing the \cancel{E}_T and $\theta_{i,\bar{i}}$ cuts to the $\theta_{i,\bar{i}}$ cuts alone are 0.50 and 0.44 for 10 TeV and 30 TeV, which further reduces the SM cross sections to 1.32 fb and 1.59 fb, where again we include the semileptonic branching ratio. This sizable suppression from the \cancel{E}_T cut is as expected as from Fig. 4. For illustration, in Table IX, we have listed the values of the SM cross sections in the semileptonically decaying channel and the $R_{1,2}$ in different bins of $m_{t\bar{t}}$ for the VBF production of top quark pair after all the preliminary cuts in Eqs. (34)–(36) and (38)

TABLE IX. The SM cross sections and the R values for anomalous top Yukawa coupling in the process $\mu^+\mu^- \rightarrow t\bar{t}v\bar{v}, t\bar{t}h\nu\bar{\nu}$ after all the preliminary cuts in Eqs. (34)–(36) and (38) with semileptonic decay for $t\bar{t}$, and $b\bar{b}$ decay for the Higgs boson in different invariant mass bins at the 30 TeV muon collider.

$m(t\bar{t})$ (TeV)	σ_{SM} (fb)	R_1	R_2
0–1	1.28	−0.0803	1.33
1–5	0.325	−0.220	12.3
5–10	0.00538	−0.155	157
10–15	4.17×10^{-4}	−0.152	468
15–20	5.21×10^{-5}	−0.163	886
20–25	6.36×10^{-6}	−0.0608	1199
25–30	1.06×10^{-6}	−0.00202	355

$m(t\bar{t}h)$ (TeV)	σ_{SM} (fb)	R_1	R_2
0–1	1.10×10^{-3}	5.75	15.5
1–5	2.74×10^{-3}	7.73	320
5–10	1.72×10^{-4}	26.8	9090
10–15	2.14×10^{-5}	49.8	51400
15–20	3.48×10^{-6}	72.8	147000
20–25	7.44×10^{-7}	58.7	186000
25–30	1.16×10^{-7}	16.5	76500

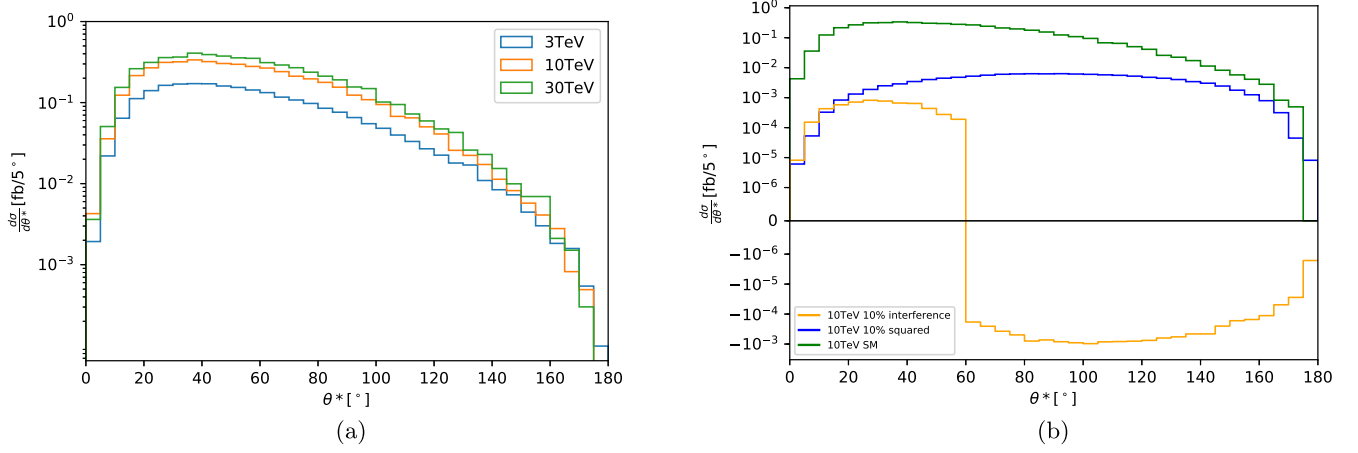


FIG. 5. The distributions of θ^* for the SM (a) and $\delta_{t\bar{t}h} = 10\%$ (b) after the all the preliminary cuts in Eqs. (34)–(36) and (38). Note that θ^* is the angle between the top and the W^+ in the W^+W^- center-of-mass frame.

at the 30 TeV muon collider. We can see that there is no energy growing behavior for the interference term, as expected from the previous analytical study. On the other hand, we do see the R value for the squared term possesses larger values at higher energy bins. For comparison, we have also presented the SM cross section R values for the process $\mu^+\mu^- \rightarrow t\bar{t}h\nu\bar{\nu}$ with semileptonically decaying top quark pair and Higgs decaying to the bottom quark pair at the 30 TeV muon collider. We can see that there is indeed energy growing behavior for the linear term.

As discussed in previous sections and also shown in Fig. 5, the scattering angle in the partonic center-of-mass frame θ^* can be used to enhance the sensitivity to the top Yukawa coupling. Here we have used an asterisk to distinguish between the polar angle of the top quark in the W^+W^- frame and the polar angle in the $\mu^+\mu^-$ frame. Furthermore, in determining the scattering angle θ^* in the partonic frame, we assume that the neutrinos are collinear with the muon beams. To be explicit, the scattering angle θ^* can be obtained from the kinematical variables in the lab frame as follows:

$$\tan \theta^* = \frac{\sqrt{p_{t,x}^2 + p_{t,y}^2} m_{t\bar{t}}}{-E_t \vec{p}_{t\bar{t}} + p_{t,z} E_{t\bar{t}}}, \quad (39)$$

where $p_{t,x}$ is the x component of the momentum of the top quark and similarly for the $p_{t,y}, p_{t,z}$. $m_{t\bar{t}}$ is the invariant mass of the top quark pair and $(E_{t\bar{t}}, \vec{p}_{t\bar{t}})$ is the four-momentum of the top quark pair. Here we have used the

fact that the transverse momentum of the top quark is the same in both the frame, while the z component of the momentum of the top quark in the partonic frame is obtained by a boost.

In addition to the invariant mass bins of the top quark pair in Table IX, we also divide the scattering angle θ^* into six bins with bin width of 30° . The corresponding cross sections and R values in each two-dimensional bin are shown in Tables XII–XV respectively in Appendix A. In order to take into account the reconstruction efficiencies of the semileptonically decaying top quark pair, we have extracted the numbers from the analysis of top quark pair production at 380 GeV, 1.4 TeV, and 3 TeV center-of-mass energy of CLIC [52]. The results are listed in Table X. We will use the following values for the reconstruction efficiencies for different $m_{t\bar{t}}$ bins:

$$[0, 1] \text{ TeV: } 64\%, \quad \text{all other bins: } 33\%, \quad (40)$$

and assume that the SM reducible backgrounds have been reduced to a negligible level. Similar efficiencies apply to the bins of $m_{t\bar{t}h}$ for the process $\mu^+\mu^- \rightarrow t\bar{t}h\nu\bar{\nu}$ with the Higgs boson decaying into bottom quark pair $h \rightarrow b\bar{b}$ with a branching ratio of 58% [56,57].

IV. RESULTS AND DISCUSSION

We follow the procedure in Appendix C to construct the likelihood functions by combining all the two-dimensional bins defined in Tables XII and XIII for 10 TeV, 30 TeV muon collider correspondingly. The integrated luminosity

TABLE X. Efficiencies from CLIC analysis of the semileptonically decaying channel with $P(e^-) = -80\%$ [52].

\sqrt{s}	380 GeV	1.4 TeV ($\sqrt{s} \geq 1.2$ TeV)	3 TeV ($\sqrt{s} \geq 2.6$ TeV)
$\epsilon_{\text{eff}}(e^+e^- \rightarrow t\bar{t} \rightarrow qqql\nu)$	64%	37%	33%

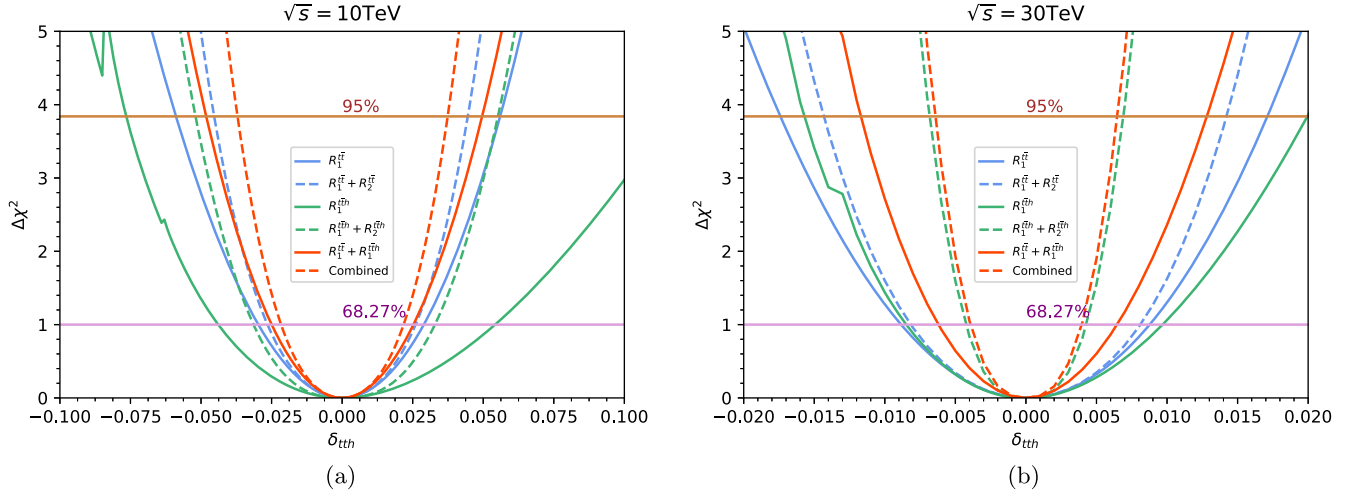


FIG. 6. $\Delta\chi^2$ plot as a function of anomalous top Yukawa coupling δ_{tth} for processes $\mu^+\mu^- \rightarrow t\bar{t}\nu\bar{\nu}$ and $\mu^+\mu^- \rightarrow t\bar{t}\nu\bar{\nu}h$ at 10 TeV (a) and 30 TeV (b) muon collider. Here $R_1(R_2)$ denotes the interference term and the squared term respectively. (a) $\mu^+\mu^- \rightarrow t\bar{t}\nu\bar{\nu}$ with $\sqrt{s} = 10$ TeV and $L = 10$ ab^{-1} . (b) $\mu^+\mu^- \rightarrow t\bar{t}\nu\bar{\nu}$ with $\sqrt{s} = 30$ TeV and $L = 90$ ab^{-1} .

is assumed to be 10 (90) ab^{-1} at the 10 (30) TeV muon collider. The $\Delta\chi^2$ as functions of the anomalous top Yukawa coupling δ_{tth} for the semileptonically decaying channels of the $t\bar{t}\nu\bar{\nu}$, $t\bar{t}h\nu\bar{\nu}$ are presented in Fig. 6. For each process, we have considered two cases: with only the linear term R_1 and with both the linear term R_1 and the quadratic term R_2 . The 95% CL interval for the δ_{tth} for different scenarios is shown in Table XI. We find that owing to the lack of energy growing behaviors in the $t\bar{t}\nu\bar{\nu}$, the expected sensitivity on the anomalous top Yukawa coupling δ_{tth} is not majorly affected by the inclusion of the quadratic term at both 10 TeV and 30 TeV. In contrast, for the $t\bar{t}h\nu\bar{\nu}$, the

quadratic terms can make a big difference (a factor of 2–3) on the top Yukawa coupling sensitivity, which is a reflection of the energy growing effects. For this process, a dedicated study should be provided to address the issue of the effective field theory breaking down, which we leave for future work. Here we are focusing on the results obtained by including the linear term R_1 only. At the 10 (30) TeV muon collider, the 95% CL on the anomalous coupling δ_{tth} from $t\bar{t}\nu\bar{\nu}$ reads as 5.6% (1.7%), which is generally in agreement with the results of [26]. These can be compared with 4% and 2% projections at 95% CL for the HE-LHC under the base and optimal scenarios

TABLE XI. 95% CL on the anomalous top Yukawa coupling δ_{tth} for different scenarios at the 10 TeV and 30 TeV muon collider.

$\sqrt{S_{\mu^+\mu^-}}$	Process	Sensitivity
10 TeV @ 10 ab^{-1}	$t\bar{t}\nu\bar{\nu} R_1$	[−5.9%, 5.6%]
	$t\bar{t}\nu\bar{\nu} R_1 + R_2$	[−4.5%, 4.5%]
	$t\bar{t}h\nu\bar{\nu} R_1$	[−7.6%, 12%]
	$t\bar{t}h\nu\bar{\nu} R_1 + R_2$	[−5.2%, 5.5%]
	$t\bar{t}\nu\bar{\nu} + t\bar{t}h\nu\bar{\nu} R_1$	[−4.8%, 5.0%]
	$t\bar{t}\nu\bar{\nu} + t\bar{t}h\nu\bar{\nu} R_1 + R_2$	[−3.7%, 3.7%]
30 TeV @ 90 ab^{-1}	$t\bar{t}\nu\bar{\nu} R_1$	[−1.7%, 1.7%]
	$t\bar{t}\nu\bar{\nu} R_1 + R_2$	[−1.4%, 1.4%]
	$t\bar{t}h\nu\bar{\nu} R_1$	[−1.6%, 2.0%]
	$t\bar{t}h\nu\bar{\nu} R_1 + R_2$	[−0.68%, 0.69%]
	$t\bar{t}\nu\bar{\nu} + t\bar{t}h\nu\bar{\nu} R_1$	[−1.2%, 1.3%]
	$t\bar{t}\nu\bar{\nu} + t\bar{t}h\nu\bar{\nu} R_1 + R_2$	[−0.64%, 0.65%]
Other colliders		
14 TeV HL-LHC @ 3 ab^{-1}	$t\bar{t}h \rightarrow$ multiple leptons	6.9% [59]
1.4 TeV CLIC @ 1.5 ab^{-1}	$t\bar{t}h \rightarrow 6j + b\bar{b}, \ell\nu 4j + b\bar{b}$	7.4% [52]
100 TeV collider @ 20 ab^{-1}	$t\bar{t}h \rightarrow \ell\nu 4j + b\bar{b}$	2% [60]

respectively [59] as well as the 2% projection at a 100 TeV collider [60], which are also listed in Table XI. For the process $t\bar{t}h\nu\bar{\nu}$, without worrying about the issues of EFT mentioned earlier, we find that the result is comparable with $t\bar{t}\nu\bar{\nu}$, especially at 30 TeV muon collider. It deserves further detailed study, which we leave for future work. Before we conclude, we would like to comment on the prospects on the measurement of the CP -phase top Yukawa coupling ξ_{htt} , which parametrize the CP -violating part of the top Yukawa coupling [61]:

$$\mathcal{L}_{htt} = -\frac{m_t}{v}(1 + \delta_{tth})\bar{t}(\cos \xi_{htt} + i \sin \xi_{htt}\gamma_5)t. \quad (41)$$

Potential observables in the process $t\bar{t}h\nu_\mu\bar{\nu}_\mu$ which are sensitive to the CP -phase ξ_{htt} include the azimuthal angle between the $t\bar{t}$ plane and the $\mu^+\mu^-$ plane and the correlated angular distributions of decay products of top and anti-top [61–63]. We leave the detailed study for future possible work.

V. CONCLUSION

In this paper, we have performed a detailed analysis about the measurement of the top Yukawa coupling at the high energy muon collider by studying the process $\mu^+\mu^- \rightarrow t\bar{t}\nu\bar{\nu}$. In particular, we have studied the energy scaling behavior of statistical signal significance S/\sqrt{B} for the subprocess $W^+W^- \rightarrow t\bar{t}$ and for the full processes at the muon collider by employing the effective W -boson approximation. In addition, we have presented the explicit formulas for the helicity amplitudes for the subprocess $W^+W^- \rightarrow t\bar{t}$ in the presence of anomalous couplings, where for completeness, we have also included anomalous triple gauge boson couplings and anomalous gauge-boson-fermions couplings. The high energy limits of the different helicity amplitudes are shown in Tables I and II, whereas the threshold behaviors are given in Tables IV and V. We have found that the sensitivity on the anomalous top Yukawa coupling δ_{tth} decreases as the energy of the bin increases as shown in Eq. (24). This is partially due to the fact that the SM amplitude for the helicity configurations $(0, 0, \pm\frac{1}{2}, \pm\frac{1}{2})$ scales like m_t/\hat{E} . As a result, the interference between the SM and BSM amplitudes will stay constant instead of growing linearly with \hat{E} . Secondly, the suppression of the parton luminosity $\Phi_{W^+W^-}(\tau)$ at high τ also reduces the signal significance S/\sqrt{B} at high energy bins. As a byproduct, we also found that in the case of triple-gauge-boson couplings $\delta\kappa_{Z,\gamma}$ and the gauge-boson-fermion couplings $\delta_{Wtb}, \delta_{Zu_L}, \delta_{Zu_R}$, the statistical signal significance mildly increases for small values of τ , mildly decreases for intermediate values of τ , and decreases at large τ values.

The semianalytical analysis has been confirmed by our numerical simulation, where we studied the prospects on the top Yukawa coupling measurement at 10 TeV and

30 TeV muon colliders. We have imposed the basic selection cuts in Eqs. (34)–(36) and (38) and focused on the semileptonically decaying channel of the top quark pair. The reconstruction efficiencies in this channel have been extracted from the CLIC analysis for different stages. Similar efficiencies are also applied to the $t\bar{t}h\nu_\mu\bar{\nu}_\mu$ process, where the Higgs boson is assumed to decay into a bottom quark pair. Furthermore, we used the distribution of the scattering angle in the partonic center-of-mass frame for the $t\bar{t}\nu_\mu\bar{\nu}_\mu$ to enhance sensitivity. The precision on the anomalous top Yukawa coupling at the 95% CL is projected to be 5.6% (1.7%) for VBF production of a top quark pair at a 10 (30) TeV muon collider. The precision from VBF production of $t\bar{t}h$ is comparable to the top quark pair, but is sensitive to contributions from the quadratic term. Therefore, it demands further detailed study, which we leave for future possible work.

ACKNOWLEDGMENTS

We would like to thank Markus Luty for the collaboration in the early stage of the project. The work of M. C. and D. L. was supported by DOE Grant No. DE-SC-0009999.

APPENDIX A: CROSS SECTIONS, THE R VALUES, AND ERRORS

In this appendix, we list the cross sections and the R values for the two-dimensional bins in terms of $m_{\bar{t}\bar{t}}, \theta^*$. The cross sections are presented in Table XII for the 10 TeV muon collider and in Table XIII for the 30 TeV muon collider. The R values are given in Table XIV for the 10 TeV muon collider and in Table XV for the 30 TeV muon collider. The errors in the tables are associated with the limited number of events generated by MadGraph5 [64], and we describe how to obtain them in the following. Note that we do not take into account the errors when we make the projections for the top Yukawa coupling measurement.

The cross section of a given process for some set of cuts is

$$\sigma = \frac{\sum_i w_i}{N}, \quad (A1)$$

where the w_i are the weights of events that remain after the cuts and N is the total number of events in the run.¹⁰ In the case where all events have positive weight, the error is the familiar $\frac{1}{\sqrt{N}}$. However, the error increases when roughly half of the events have negative weight.

To determine the error in the cross section, we begin by writing the cross section of each individual run as

¹⁰In order to find cross sections across multiple Les Houches Event (LHE) files with different cuts, we simply sum the individual over cross sections.

TABLE XII. The SM cross sections in [fb] in the two dimensional bins $m_{\tilde{t}}, \theta^*$ for the process $\mu^+\mu^- \rightarrow t\bar{t}\nu\bar{\nu}$ after all the preliminary cuts in Eqs. (34)–(36) and (38).

$m_{\tilde{t}}[\text{TeV}]/\theta^* [^\circ]$ [fb]	[0, 30]	[30, 60]	[60, 90]	[90, 120]	[120, 150]	[150, 180]
[0, 1]	0.670 ± 0.00025	1.22 ± 0.00039	1.48 ± 0.00049	0.503 ± 0.00038	0.0933 ± 0.00022	0.0145 ± 0.00011
[1, 2]	$0.234 \pm 8.5 \times 10^{-5}$	0.233 ± 0.00012	0.142 ± 0.00012	$0.0403 \pm 8.3 \times 10^{-5}$	$0.0122 \pm 5.8 \times 10^{-5}$	$0.00270 \pm 3.5 \times 10^{-5}$
[2, 4]	$0.0449 \pm 2.3 \times 10^{-5}$	$0.0322 \pm 2.6 \times 10^{-5}$	$0.0141 \pm 2.3 \times 10^{-5}$	$4.61 \times 10^{-3} \pm 1.6 \times 10^{-5}$	$1.95 \times 10^{-3} \pm 1.3 \times 10^{-5}$	$6.52 \times 10^{-4} \pm 9.0 \times 10^{-6}$
[4, 6]	$3.08 \times 10^{-3} \pm 2.2 \times 10^{-6}$	$1.76 \times 10^{-3} \pm 2.3 \times 10^{-6}$	$6.49 \times 10^{-4} \pm 1.8 \times 10^{-6}$	$2.78 \times 10^{-4} \pm 1.4 \times 10^{-6}$	$1.40 \times 10^{-4} \pm 1.1 \times 10^{-6}$	$8.01 \times 10^{-5} \pm 8.2 \times 10^{-7}$
[6, 8]	$2.46 \times 10^{-4} \pm 1.9 \times 10^{-7}$	$1.23 \times 10^{-4} \pm 1.9 \times 10^{-7}$	$5.56 \times 10^{-5} \pm 1.5 \times 10^{-7}$	$3.16 \times 10^{-5} \pm 1.1 \times 10^{-7}$	$2.43 \times 10^{-5} \pm 8.8 \times 10^{-8}$	$1.73 \times 10^{-5} \pm 6.9 \times 10^{-8}$
[8, 10]	$8.33 \times 10^{-6} \pm 5.2 \times 10^{-9}$	$6.71 \times 10^{-6} \pm 5.2 \times 10^{-9}$	$6.47 \times 10^{-6} \pm 3.9 \times 10^{-9}$	$6.21 \times 10^{-6} \pm 3.0 \times 10^{-9}$	$7.13 \times 10^{-6} \pm 2.4 \times 10^{-9}$	$9.54 \times 10^{-6} \pm 1.9 \times 10^{-9}$

TABLE XIII. The SM cross sections in the two dimensional bins $m_{\tilde{t}}, \theta^*$ for the process $\mu^+\mu^- \rightarrow t\bar{t}\nu\bar{\nu}$ at 30 TeV muon collider after all the preliminary cuts in Eqs. (34)–(36) and (38).

$m_{\tilde{t}}[\text{TeV}]/\theta^* [^\circ]$ [fb]	[0,30]	[30,60]	[60,90]	[90,120]	[120,150]	[150,180]
[0, 1]	0.641 ± 0.00033	1.28 ± 0.00055	1.95 ± 0.00080	0.61 ± 0.00060	0.085 ± 0.00031	0.0119 ± 0.00014
[1, 5]	0.368 ± 0.00021	0.376 ± 0.00026	0.314 ± 0.00031	0.0821 ± 0.00022	0.0174 ± 0.00013	0.00375 ± 0.000083
[5, 10]	$8.33 \times 10^{-3} \pm 1.2 \times 10^{-5}$	$6.40 \times 10^{-3} \pm 1.4 \times 10^{-5}$	$3.03 \times 10^{-3} \pm 1.3 \times 10^{-5}$	$9.68 \times 10^{-4} \pm 9.0 \times 10^{-6}$	$3.90 \times 10^{-4} \pm 6.6 \times 10^{-6}$	$1.27 \times 10^{-4} \pm 4.8 \times 10^{-6}$
[10, 15]	$7.52 \times 10^{-4} \pm 1.5 \times 10^{-6}$	$4.55 \times 10^{-4} \pm 1.7 \times 10^{-6}$	$1.73 \times 10^{-4} \pm 1.3 \times 10^{-6}$	$6.71 \times 10^{-5} \pm 9.8 \times 10^{-7}$	$3.22 \times 10^{-5} \pm 7.7 \times 10^{-7}$	$1.41 \times 10^{-5} \pm 5.8 \times 10^{-7}$
[15, 20]	$9.77 \times 10^{-5} \pm 2.2 \times 10^{-7}$	$5.02 \times 10^{-5} \pm 2.3 \times 10^{-7}$	$1.97 \times 10^{-5} \pm 1.8 \times 10^{-7}$	$9.15 \times 10^{-6} \pm 1.3 \times 10^{-7}$	$5.65 \times 10^{-6} \pm 1.1 \times 10^{-7}$	$3.17 \times 10^{-6} \pm 8.3 \times 10^{-8}$
[20, 25]	$1.02 \times 10^{-5} \pm 2.4 \times 10^{-8}$	$5.29 \times 10^{-6} \pm 2.4 \times 10^{-8}$	$2.80 \times 10^{-6} \pm 1.8 \times 10^{-8}$	$1.83 \times 10^{-6} \pm 1.4 \times 10^{-8}$	$1.46 \times 10^{-6} \pm 1.1 \times 10^{-8}$	$1.12 \times 10^{-6} \pm 8.5 \times 10^{-9}$
[25, 30]	$4.47 \times 10^{-7} \pm 7.2 \times 10^{-10}$	$4.81 \times 10^{-7} \pm 7.2 \times 10^{-10}$	$5.44 \times 10^{-7} \pm 5.4 \times 10^{-10}$	$5.93 \times 10^{-7} \pm 4.1 \times 10^{-10}$	$7.04 \times 10^{-7} \pm 3.3 \times 10^{-10}$	$1.02 \times 10^{-6} \pm 2.6 \times 10^{-10}$

$$\sigma = \sigma_+ + \sigma_- = \frac{wm_1}{N} - \frac{wm_2}{N}, \quad (\text{A2})$$

where N denotes the total number of events in the LHE file, m_1 is the total number of positive weight events, m_2 the number of negative weights, and w is the absolute value of the weight. For the case where no cuts are imposed, we have that $m_1 + m_2 = N$, but this is not the case in general. Taking $\frac{\delta\sigma_+}{\sigma_+} = \frac{1}{\sqrt{m_1}}$ and similar for σ_- , we have that

$$\delta\sigma^2 = \delta\sigma_+^2 + \delta\sigma_-^2 = \frac{w^2(m_1 + m_2)}{N^2}$$

$$\delta\sigma = \sigma \frac{\sqrt{m_1 + m_2}}{m_1 - m_2}, \quad (\text{A3})$$

which is the error for each LHE file. The second line of Eq. (A3) assumes that $m_1 \neq m_2$. Since the total cross

section of a given bin is found by summing up the individual cross sections of the LHE files, we have that

$$\delta\sigma_{\text{bin}}^2 = \sum_i \delta\sigma_i^2. \quad (\text{A4})$$

APPENDIX B: HELICITY AMPLITUDES FOR $W^+W^- \rightarrow t\bar{t}$

In this appendix, we present the full helicity amplitudes for the subprocess $W^+W^- \rightarrow t\bar{t}$:

$$\mathcal{M}(W^+(p_1)W^-(p_2) \rightarrow t(p_3)\bar{t}(p_4)) = \mathcal{M}^\gamma + \mathcal{M}^Z + \mathcal{M}^h + \mathcal{M}^t, \quad (\text{B1})$$

where $\mathcal{M}^{\gamma,Z,h}$ denotes the s -channel contribution with γ, Z, h particles as internal lines and \mathcal{M}^t corresponds to the t -channel contribution. Since the initial particles have the

TABLE XIV. R -values in the two dimensional bins $m_{\bar{t}\bar{t}}, \theta^*$ for the process $\mu^+\mu^- \rightarrow t\bar{t}\nu\bar{\nu}$ after all the preliminary cuts in Eqs. (34)–(36) and (38).

$m_{\bar{t}\bar{t}}[\text{TeV}]/\theta^* [^\circ]$	[0, 30]	[30, 60]	[60, 90]	[90, 120]	[120, 150]	[150, 180]
[0, 1]						
R_1	0.209 ± 0.070	0.143 ± 0.052	-0.0484 ± 0.047	-0.647 ± 0.081	-1.54 ± 0.19	-2.60 ± 0.48
R_2	0.279 ± 0.67	0.563 ± 0.51	1.16 ± 0.48	3.40 ± 0.82	7.20 ± 1.7	12.8 ± 4.1
[1, 2]						
R_1	-0.0314 ± 0.055	-0.0778 ± 0.055	-0.266 ± 0.071	-0.827 ± 0.13	-1.79 ± 0.24	-3.81 ± 0.51
R_2	1.29 ± 0.57	3.06 ± 0.54	8.43 ± 0.70	29.9 ± 1.4	58.3 ± 2.3	110 ± 4.5
[2, 4]						
R_1	-0.0124 ± 0.052	-0.116 ± 0.061	-0.313 ± 0.092	-0.790 ± 0.16	-1.33 ± 0.25	-2.68 ± 0.43
R_2	5.28 ± 0.54	12.8 ± 0.57	36.2 ± 0.89	110 ± 1.7	212 ± 2.7	362 ± 6.2
[4, 6]						
R_1	-0.0109 ± 0.050	-0.127 ± 0.066	-0.331 ± 0.11	-0.481 ± 0.17	-0.842 ± 0.23	-1.25 ± 0.31
R_2	17.1 ± 0.53	44.7 ± 0.60	128 ± 1.1	297 ± 2.2	556 ± 4.9	649 ± 7.1
[6, 8]						
R_1	-0.0171 ± 0.049	-0.0997 ± 0.069	-0.205 ± 0.10	0.211 ± 0.14	-0.252 ± 0.16	-0.218 ± 0.18
R_2	33.7 ± 0.52	95.5 ± 0.65	207 ± 1.1	365 ± 1.9	478 ± 2.4	479 ± 2.5
[8, 10]						
R_1	0.0116 ± 0.073	-0.0316 ± 0.082	-0.0188 ± 0.083	-0.0103 ± 0.085	0.00346 ± 0.079	0.00128 ± 0.068
R_2	47.9 ± 0.79	81.3 ± 0.77	82.1 ± 0.80	85.2 ± 0.88	76.7 ± 0.86	41.7 ± 0.62

TABLE XV. R values in the two-dimensional bins $m_{\bar{t}\bar{t}}, \theta^*$ for the process $\mu^+\mu^- \rightarrow t\bar{t}\nu\bar{\nu}$ after all the preliminary cuts in Eqs. (34)–(36) and (38).

$m_{\bar{t}\bar{t}}[\text{TeV}]/\theta^* [^\circ]$	[0, 30]	[30, 60]	[60, 90]	[90, 120]	[120, 150]	[150, 180]
[0, 1]						
R_1	0.197 ± 0.0056	0.137 ± 0.0044	-0.0365 ± 0.0041	-0.694 ± 0.012	-1.66 ± 0.057	-2.88 ± 0.24
R_2	0.286 ± 0.0078	0.508 ± 0.0072	1.08 ± 0.0091	3.55 ± 0.042	9.70 ± 0.32	22.3 ± 2.1
[1, 5]						
R_1	-0.00399 ± 0.0057	-0.0849 ± 0.0071	-0.287 ± 0.0099	-0.956 ± 0.030	-2.05 ± 0.10	-4.76 ± 0.39
R_2	2.66 ± 0.028	5.50 ± 0.049	12.8 ± 0.11	48.0 ± 0.71	145 ± 5.2	368 ± 30
[5, 10]						
R_1	-0.0171 ± 0.015	-0.101 ± 0.022	-0.236 ± 0.041	-0.824 ± 0.095	-0.882 ± 0.17	-2.59 ± 0.41
R_2	32.4 ± 0.30	92.4 ± 0.94	242 ± 3.3	654 ± 14	1459 ± 54	3465 ± 259
[10, 15]						
R_1	-0.00494 ± 0.020	-0.131 ± 0.037	-0.346 ± 0.077	-0.732 ± 0.15	-1.09 ± 0.24	-1.35 ± 0.42
R_2	99.5 ± 0.84	335 ± 3.6	890 ± 14	1946 ± 45	4012 ± 138	7773 ± 460
[15, 20]						
R_1	-0.0605 ± 0.023	-0.129 ± 0.046	-0.351 ± 0.092	0.406 ± 0.15	-0.914 ± 0.19	-0.639 ± 0.26
R_2	195 ± 1.5	738 ± 7.8	1770 ± 28	3159 ± 65	5080 ± 133	9193 ± 386
[20, 25]						
R_1	-0.0195 ± 0.023	-0.0786 ± 0.045	-0.0399 ± 0.064	-0.0314 ± 0.074	-0.201 ± 0.075	-0.268 ± 0.076
R_2	321 ± 2.5	1166 ± 13	1942 ± 27	2519 ± 40	3201 ± 56	4070 ± 95
[25, 30]						
R_1	0.0111 ± 0.016	-0.00137 ± 0.015	-0.0253 ± 0.010	-0.00295 ± 0.0069	0.00193 ± 0.0047	0.00218 ± 0.0026
R_2	339 ± 4.3	568 ± 7.7	488 ± 6.3	373 ± 4.3	303 ± 3.1	214 ± 2.2

same masses as well as the final particles, the energies of the top quarks are equal to that of the W bosons in the partonic center-of-mass frame:

$$\hat{E}_t = \hat{E}_W = \frac{\sqrt{\hat{s}}}{2}. \quad (\text{B2})$$

The other Mandelstam variables \hat{t}, \hat{u} can be written as functions of \hat{s} :

$$\begin{aligned} \hat{t} &= \frac{\hat{s}}{4}(-\beta_t^2 - \beta_W^2 + 2\beta_t\beta_W \cos\theta), \\ \hat{u} &= \frac{\hat{s}}{4}(-\beta_t^2 - \beta_W^2 - 2\beta_t\beta_W \cos\theta), \end{aligned} \quad (\text{B3})$$

where the velocities of the W bosons and the top quarks are given by

$$\beta_{W,t} = \sqrt{1 - \frac{4m_{W,t}^2}{\hat{s}}}. \quad (\text{B4})$$

Here the scattering angle θ in the partonic center-of-mass frame is the polar angle between the outgoing top quark and

the incoming W^+ gauge boson. The z -axis is chosen as the direction of the W^+ spatial momentum. The azimuthal angles of the top quark and the antitop quark are chosen as

$$\varphi_t = 0, \quad \varphi_{\bar{t}} = \pi, \quad (\text{B5})$$

which will fix the possible i factors in the polarization functions of the antitop quarks. We will present the helicity amplitudes in terms of the Wigner d functions [65]:

$$\begin{aligned} \mathcal{M}_{h_1 h_2; h_3 h_4} &= \tilde{\mathcal{M}}_{h_1 h_2; h_3 h_4}(\theta)(h_3 - h_4 + \delta_{h_3 h_4}) \\ &\times (-1)^{h_2} d_{\Delta h_{12}, \Delta h_{34}}^{J_0}(\theta), \end{aligned} \quad (\text{B6})$$

with

$$\begin{aligned} \Delta h_{12} &= h_1 - h_2, \quad \Delta h_{34} = h_3 - h_4, \\ J_0 &= \max(|\Delta h_{12}|, |\Delta h_{34}|), \end{aligned} \quad (\text{B7})$$

and to make results more compact, we have also extracted some sign factors for convenience. The relevant d functions are listed as follows [57]:

$$\begin{aligned} d_{1,1}^1 &= d_{-1,-1}^1 = \frac{1}{2}(1 + \cos\theta), & d_{1,-1}^1 &= d_{-1,1}^1 = \frac{1}{2}(1 - \cos\theta), \\ d_{1,0}^1 &= -d_{-1,0}^1 = -\frac{\sin\theta}{\sqrt{2}}, \\ d_{1,2}^2 &= -d_{-1,-2}^2 = \frac{1}{2}\sin\theta(1 + \cos\theta), & d_{1,-2}^2 &= -d_{-1,2}^2 = -\frac{1}{2}\sin\theta(1 - \cos\theta), \end{aligned} \quad (\text{B8})$$

which satisfy the following identities:

$$d_{m',m}^j = (-1)^{m-m'} d_{m,m'}^j = d_{-m,-m'}^j. \quad (\text{B9})$$

The top Yukawa coupling modification is parametrized as

$$\mathcal{L}_{h\bar{t}t} = -\frac{m_t}{v}(1 + \delta_{th})h\bar{t}t. \quad (\text{B10})$$

For future studies, we have also included the CP -even aTGC, which are parametrized as follows [65,66]:

$$\begin{aligned} \mathcal{L}_{WWV}/g_{WWV}^{\text{SM}} &= ig_1^V(W_{\mu\nu}^+ W^{-\mu} V^\nu - W_{\mu\nu}^- W^{+\mu} V^\nu) \\ &+ i\kappa_V W_\mu^+ W_\nu^- V^{\mu\nu} + i\frac{\lambda_V}{m_W^2} W_{\lambda\mu}^+ W^{-\mu}{}_\nu V^{\nu\lambda}, \end{aligned} \quad (\text{B11})$$

where $W_{\mu\nu}^\pm = \partial_\mu W_\nu^\pm - \partial_\nu W_\mu^\pm$ and $V = \gamma, Z$. The SM values of the TGCs read as

$$g_{WW\gamma}^{\text{SM}} = e, \quad g_{WWZ}^{\text{SM}} = g \cos\theta_W, \quad (\text{B12})$$

where θ_W is the weak mixing angle. The unbroken electromagnetism fixes g_1^Z to be 1. So we are left with five anomalous TGC couplings: $\delta g_1^Z, \delta\kappa_Z, \delta\kappa_\gamma, \lambda_Z, \lambda_\gamma$ defined as $\delta g_1^Z = g_1^Z - 1, \delta\kappa_V = \kappa_V - 1$. At dimension-six SMEFT, they are further related by the following identities [67]:

$$\delta\kappa_Z = \delta g_1^Z - \tan^2\theta_W \delta\kappa_\gamma, \quad \lambda_Z = \lambda_\gamma. \quad (\text{B13})$$

We also take into account the contributions from the possible modifications of the top electroweak couplings and the Higgs gauge boson coupling:

$$\begin{aligned} \delta_{Wtb} &= \frac{g_{Wtb}}{g_{Wtb}^{\text{SM}}} - 1, & \delta_{Zt_L} &= \frac{g_{Zt_L}}{g_{Zt_L}^{\text{SM}}} - 1, \\ \delta_{Zt_R} &= \frac{g_{Zt_R}}{g_{Zt_R}^{\text{SM}}} - 1, & \delta_{hWW} &= \frac{g_{hWW}}{g_{hWW}^{\text{SM}}} - 1, \end{aligned} \quad (\text{B14})$$

with their SM values as follows:

$$g_{Wt}^{\text{SM}} = \frac{g}{\sqrt{2}}, \quad g_{Zt_L}^{\text{SM}} = \frac{g}{\cos\theta_W} \left(\frac{1}{2} - \frac{2}{3} \sin^2\theta_W \right), \quad g_{Zt_R}^{\text{SM}} = -\frac{2g\sin^2\theta_W}{3\cos\theta_W}, \quad g_{hWW}^{\text{SM}} = \frac{2m_W^2}{v}. \quad (\text{B15})$$

Note that we are working in the broken phase of electroweak symmetry. All the anomalous couplings can be rewritten in terms of the Wilson coefficients of the dimension-six operators:

$$\begin{aligned} \delta_{hWW} &= -\frac{c_H}{2} \frac{v^2}{\Lambda^2}, & \delta_{tth} &= -\xi \left(\frac{c_H}{2} + c_{y_t} \right) \\ \delta g_1^Z &= -\frac{c_W + c_{HW}}{\cos^2\theta_W} \frac{m_W^2}{\Lambda^2}, & \delta\kappa_\gamma &= -(c_{HW} + c_{HB}) \frac{m_W^2}{\Lambda^2}, & \lambda_Z = \lambda_\gamma &= c_{3W} \frac{m_W^2}{\Lambda^2} \\ \delta_{Wtb} &= \frac{g}{\sqrt{2}} c_L^{(3)q} \frac{4m_W^2}{\Lambda^2}, & \delta_{Zt_L} &= -\frac{g}{c_W} \frac{2m_W^2}{\Lambda^2} (c_L^q - c_L^{(3)q}), & \delta_{Zt_R} &= -\frac{g}{c_W} \frac{2m_W^2}{\Lambda^2} c_R^t, \end{aligned} \quad (\text{B16})$$

where Λ is the cutoff scale and the SMEFT operators are given by

$$\begin{aligned} \mathcal{O}_H &= \frac{1}{2} \partial_\mu (H^\dagger H) \partial^\mu (H^\dagger H), & \mathcal{O}_{y_t} &= y_t H^\dagger H \bar{q}_L H t_R \\ \mathcal{O}_W &= \frac{ig}{2} (H^\dagger \sigma^a \overleftrightarrow{D}^\mu H) D^\nu W_{\mu\nu}^a, & \mathcal{O}_B &= \frac{ig'}{2} (H^\dagger \overleftrightarrow{D}^\mu H) \partial^\nu B_{\mu\nu} \\ \mathcal{O}_{HW} &= ig (D^\mu H)^\dagger \sigma^a (D^\nu H) W_{\mu\nu}^a, & \mathcal{O}_{HB} &= ig' (D^\mu H)^\dagger (D^\nu H) B_{\mu\nu} \\ \mathcal{O}_{3W} &= \frac{1}{3!} g \epsilon_{abc} W_\mu^{av} W_\nu^{bw} W^{\nu\mu c}, & \mathcal{O}_L^{(3)q} &= ig^2 (H^\dagger \sigma^a \overleftrightarrow{D}_\mu H) \bar{Q}_L \sigma^a \gamma^\mu Q_L \\ \mathcal{O}_R^t &= ig^2 (H^\dagger \overleftrightarrow{D}_\mu H) \bar{u}_R \gamma^\mu u_R, & \mathcal{O}_L^q &= ig^2 (H^\dagger \overleftrightarrow{D}_\mu H) \bar{Q}_L \gamma^\mu Q_L. \end{aligned} \quad (\text{B17})$$

Now, we turn to the formulas for the helicity amplitudes. In order to list them compactly in tables, we further take some prefactors out of $\tilde{\mathcal{M}}$:

$$\begin{aligned} \tilde{\mathcal{M}}^\gamma &= i \frac{2\sqrt{2}g^2 s_W^2 \beta_W}{3} A_{h_1 h_2; h_3 h_4}^\gamma \\ \tilde{\mathcal{M}}^Z &= i\sqrt{2}g^2 \beta_W \left(\frac{1 - \Delta h_{34} \beta_t}{4} (1 + \delta_{Zt_L}) - \frac{2}{3} s_W^2 \left(1 + \frac{1 - \Delta h_{34} \beta_t}{2} \delta_{Zt_L} + \frac{1 + \Delta h_{34} \beta_t}{2} \delta_{Zt_R} \right) \right) \frac{\hat{s}}{\hat{s} - m_Z^2} A_{h_1 h_2; h_3 h_4}^Z \\ \tilde{\mathcal{M}}^h &= i \frac{g^2}{2\sqrt{2}} (1 + \delta_{tth}) (1 + \delta_{hWW}) \beta_t \frac{\hat{s}}{\hat{s} - m_h^2} A_{h_1 h_2; h_3 h_4}^h \\ \tilde{\mathcal{M}}^t &= -i \frac{g^2 (1 - \Delta h_{34} \beta_t)}{2\sqrt{2} \beta_W} (1 + \delta_{Wtb})^2 \left(B_{h_1 h_2; h_3 h_4} - \frac{1}{\beta_t^2 + \beta_W^2 - 2\beta_t \beta_W \cos\theta} C_{h_1 h_2; h_3 h_4} \right), \end{aligned} \quad (\text{B18})$$

where we have abbreviated $\sin\theta_W$ as s_W . Note that the kinematical function in front of $C_{h_1, h_2; h_3, h_4}$ is simply $\frac{\hat{s}}{4\beta}$ and we have omitted the small bottom quark mass. The results for the helicity configurations $(\mp\frac{1}{2}, \pm\frac{1}{2})$ of final top and antitop quarks are presented in Table XVI, and for other helicity configurations $(\mp\frac{1}{2}, \mp\frac{1}{2})$, they are shown in Table XVII.

APPENDIX C: STATISTICS

In order to constrain the top Yukawa coupling as shown in Fig. 6, we follow the frequentist statistics procedure

outlined in [56]. We first construct the likelihood function $L(\delta_{tth})$:

$$L(\delta_{tth}) = P(n|\delta_{tth}), \quad (\text{C1})$$

where n is the observed number of events and $P(n|\delta_{tth})$ is the probability under the hypothesis of δ_{tth} . Here we have used the Poisson distribution:

$$P(n|\delta_{tth}) = \frac{(s(\delta_{tth}) + b)^n}{n!} e^{-(s(\delta_{tth}) + b)}, \quad (\text{C2})$$

TABLE XVI. Helicity amplitude factors for $W_{h_1}^+ W_{h_2}^- \rightarrow t_{h_3} \bar{t}_{h_4}$ for $\Delta h_{34} = \mp 1$. Here $V = \gamma, Z$, and note that $\delta g_1^\gamma = 0$.

$(h_3 h_4)$	$(h_1 h_2)$	$A_{h_1 h_2; h_3 h_4}^V$	$A_{h_1 h_2; h_3 h_4}^h$	$B_{h_1 h_2; h_3 h_4}$	$C_{h_1 h_2; h_3 h_4}$
$(-\frac{1}{2} \frac{1}{2})$	$(+1 -1), (-1 +1)$	0	0	0	$-2\sqrt{2}\beta_t\beta_W$
	$(+1 +1), (-1 -1)$	$1 + \delta g_1^V + \frac{s}{2m_W^2}\lambda_V$	0	1	$\beta_t^2 - \beta_W^2$
	$(+1 0), (0 -1)$	$\frac{\sqrt{s}}{m_W} \left(1 + \frac{\delta g_1^V + \delta\kappa_V + \lambda_V}{2}\right)$	0	$\frac{\sqrt{s}}{m_W}$	$\frac{\sqrt{s}(\beta_t + \beta_W)(\beta_t - \beta_W^2)}{m_W}$
	$(-1 0), (0 +1)$	$-\frac{\sqrt{s}}{m_W} \left(1 + \frac{\delta g_1^V + \delta\kappa_V + \lambda_V}{2}\right)$	0	$-\frac{\sqrt{s}}{m_W}$	$-\frac{\sqrt{s}(\beta_t - \beta_W)(\beta_t - \beta_W^2)}{m_W}$
	$(0 0)$	$-1 - \delta g_1^V - \frac{s}{2m_W^2}(1 + \delta\kappa_V)$	0	$-\frac{s}{2m_W^2}$	$-\frac{s(\beta_t - \beta_W^2)^2}{2m_W^2}$
$(\frac{1}{2} - \frac{1}{2})$	$(+1 -1), (-1 +1)$	0	0	0	$-2\sqrt{2}\beta_t\beta_W$
	$(+1 +1), (-1 -1)$	$1 + \delta g_1^V + \frac{s}{2m_W^2}\lambda_V$	0	1	$\beta_t^2 - \beta_W^2$
	$(+1 0), (0 -1)$	$\frac{\sqrt{s}}{m_W} \left(1 + \frac{\delta g_1^V + \delta\kappa_V + \lambda_V}{2}\right)$	0	$\frac{\sqrt{s}}{m_W}$	$\frac{\sqrt{s}(\beta_t - \beta_W)(\beta_t + \beta_W^2)}{m_W}$
	$(-1 0), (0 +1)$	$-\frac{\sqrt{s}}{m_W} \left(1 + \frac{\delta g_1^V + \delta\kappa_V + \lambda_V}{2}\right)$	0	$-\frac{\sqrt{s}}{m_W}$	$-\frac{\sqrt{s}(\beta_t + \beta_W)(\beta_t + \beta_W^2)}{m_W}$
	$(0 0)$	$-1 - \delta g_1^V - \frac{s}{2m_W^2}(1 + \delta\kappa_V)$	0	$-\frac{s}{2m_W^2}$	$-\frac{s(\beta_t + \beta_W^2)^2}{2m_W^2}$

TABLE XVII. Helicity amplitude factors for $W_{h_1}^+ W_{h_2}^- \rightarrow t_{h_3} \bar{t}_{h_4}$ for $\Delta h_{34} = 0$. Here $V = \gamma, Z$, and note that $\delta g_1^\gamma = 0$.

$(h_3 h_4)$	$(h_1 h_2)$	$A_{h_1 h_2; h_3 h_4}^V$	$A_{h_1 h_2; h_3 h_4}^h$
$(-\frac{1}{2} - \frac{1}{2})$	$(+1 -1), (-1 +1)$	0	0
	$(+1 +1), (-1 -1)$	$\frac{\sqrt{2}m_t}{\sqrt{s}} \left(1 + \delta g_1^V + \frac{s}{2m_W^2}\lambda_V\right) \cos\theta$	$-\frac{\sqrt{2}m_t}{\sqrt{s}}$
	$(+1 0), (0 -1)$	$\frac{\sqrt{2}m_t}{m_W} \left(1 + \frac{\delta g_1^V + \delta\kappa_V + \lambda_V}{2}\right)$	0
	$(-1 0), (0 +1)$	$-\frac{\sqrt{2}m_t}{m_W} \left(1 + \frac{\delta g_1^V + \delta\kappa_V + \lambda_V}{2}\right)$	0
	$(0 0)$	$-\frac{\sqrt{2}m_t}{\sqrt{s}} \left(1 + \delta g_1^V + \frac{s(1 + \delta\kappa_V)}{2m_W^2}\right) \cos\theta$	$-\frac{\sqrt{2}m_t\sqrt{s}(1 + \beta_W^2)}{4m_W^2}$
$(\frac{1}{2} \frac{1}{2})$	$(+1 -1), (-1 +1)$	0	0
	$(+1 +1), (-1 -1)$	$-\frac{\sqrt{2}m_t}{\sqrt{s}} \left(1 + \delta g_1^V + \frac{s}{2m_W^2}\lambda_V\right) \cos\theta$	$\frac{\sqrt{2}m_t}{\sqrt{s}}$
	$(+1 0), (0 -1)$	$-\frac{\sqrt{2}m_t}{m_W} \left(1 + \frac{\delta g_1^V + \delta\kappa_V + \lambda_V}{2}\right)$	0
	$(-1 0), (0 +1)$	$\frac{\sqrt{2}m_t}{m_W} \left(1 + \frac{\delta g_1^V + \delta\kappa_V + \lambda_V}{2}\right)$	0
	$(0 0)$	$\frac{\sqrt{2}m_t}{\sqrt{s}} \left(1 + \delta g_1^V + \frac{s(1 + \delta\kappa_V)}{2m_W^2}\right) \cos\theta$	$\frac{\sqrt{2}m_t\sqrt{s}(1 + \beta_W^2)}{4m_W^2}$
$(h_3 h_4)$	$(h_1 h_2)$	$B_{h_1 h_2; h_3 h_4}$	$C_{h_1 h_2; h_3 h_4}$
$(-\frac{1}{2} - \frac{1}{2})$	$(+1 -1), (-1 +1)$	0	$-\frac{8m_t\beta_t\beta_W}{\sqrt{3}\sqrt{s}}$
	$(+1 +1), (-1 -1)$	$\frac{m_t(\beta_t^2 - \beta_W^2 \mp 2\beta_t\beta_W + 2\beta_t\beta_W \cos\theta)}{\sqrt{2}\sqrt{s}\beta_t\beta_W}$	$\frac{m_t(\beta_t \mp \beta_W)^2(\beta_t^2 - \beta_W^2)}{\sqrt{2}\sqrt{s}\beta_t\beta_W}$
	$(+1 0), (0 -1)$	$\frac{\sqrt{2}m_t}{m_W}$	$\frac{\sqrt{2}m_t(\beta_t \mp \beta_W)(\beta_t \pm \beta_W^2)}{m_W}$
	$(-1 0), (0 +1)$	$-\frac{\sqrt{2}m_t}{m_W}$	$-\frac{\sqrt{2}m_t(\beta_t \pm \beta_W)(\beta_t \mp \beta_W^2)}{m_W}$
	$(0 0)$	$-\frac{\sqrt{s}m_t(\beta_t^2 + \beta_W^4 + 2\beta_t\beta_W \cos\theta)}{2\sqrt{2}m_W^2\beta_t\beta_W}$	$-\frac{\sqrt{s}m_t(\beta_t^4 + \beta_W^6 - \beta_t^2(\beta_W^2 + \beta_W^4))}{2\sqrt{2}m_W^2\beta_t\beta_W}$
$(\frac{1}{2} \frac{1}{2})$	$(+1 -1), (-1 +1)$	0	$\frac{8m_t\beta_t\beta_W}{\sqrt{3}\sqrt{s}}$
	$(+1 +1), (-1 -1)$	$-\frac{m_t(\beta_t^2 - \beta_W^2 \pm 2\beta_t\beta_W + 2\beta_t\beta_W \cos\theta)}{\sqrt{2}\sqrt{s}\beta_t\beta_W}$	$-\frac{m_t(\beta_t \pm \beta_W)^2(\beta_t^2 - \beta_W^2)}{\sqrt{2}\sqrt{s}\beta_t\beta_W}$
	$(+1 0), (0 -1)$	$-\frac{\sqrt{2}m_t}{m_W}$	$-\frac{\sqrt{2}m_t(\beta_t \pm \beta_W)(\beta_t \mp \beta_W^2)}{m_W}$
	$(-1 0), (0 +1)$	$\frac{\sqrt{2}m_t}{m_W}$	$\frac{\sqrt{2}m_t(\beta_t \mp \beta_W)(\beta_t \mp \beta_W^2)}{m_W}$
	$(0 0)$	$\frac{\sqrt{s}m_t(\beta_t^2 + \beta_W^4 + 2\beta_t\beta_W \cos\theta)}{2\sqrt{2}m_W^2\beta_t\beta_W}$	$\frac{\sqrt{s}m_t(\beta_t^4 + \beta_W^6 - \beta_t^2(\beta_W^2 + \beta_W^4))}{2\sqrt{2}m_W^2\beta_t\beta_W}$

where s is the number of signal events, which is a function of δ_{th} , and b is the number of SM background events. For multibin analysis, as is the case in this paper, the total probability function is given by the product of the probability function in each bin, i.e.,

$$P(\vec{n}|\delta_{th}) = \prod_i \frac{(s_i(\delta_{th}) + b_i)^{n_i}}{n_i!} e^{-(s_i(\delta_{th}) + b_i)}. \quad (C3)$$

The χ^2 function is defined as

$$\chi^2 = -2 \ln L, \quad (C4)$$

and we will use the method of maximum likelihood to estimate the confidence interval. The $\Delta\chi^2$ as plotted in Fig. 6 is defined as

$$\Delta\chi^2 = \chi^2 - \chi^2_{\min} = 2 \ln L_{\max} - 2 \ln L, \quad (C5)$$

where L_{\max} is the maximal value of the likelihood function with given data \vec{n} . The expected sensitivity is obtained by setting the observed number of events to the SM background values $\vec{n} = \vec{b}$. The confidence interval at m standard deviation is obtained by solving the following equation:

$$\Delta\chi^2 = m^2. \quad (C6)$$

-
- [1] S. Schael *et al.* (ALEPH, DELPHI, L3, OPAL, SLD, LEP Electroweak Working Group, SLD Electroweak Group, and SLD Heavy Flavour Group Collaborations), Precision electroweak measurements on the Z resonance, *Phys. Rep.* **427**, 257 (2006).
- [2] S. Dittmaier *et al.* (LHC Higgs Cross Section Working Group), Handbook of LHC Higgs cross sections: 1. Inclusive observables, [arXiv:1101.0593](https://arxiv.org/abs/1101.0593).
- [3] J. M. Cornwall, D. N. Levin, and G. Tiktopoulos, Derivation of gauge invariance from high-energy unitarity bounds on the s matrix, *Phys. Rev. D* **10**, 1145 (1974); *Phys. Rev. D* **11**, 972(E) (1975).
- [4] D. Liu and Z. Yin, Gauge invariance from on-shell massive amplitudes and tree-level unitarity, *Phys. Rev. D* **106**, 076003 (2022).
- [5] M. Farina, G. Panico, D. Pappadopulo, J. T. Ruderman, R. Torre, and A. Wulzer, Energy helps accuracy: Electroweak precision tests at hadron colliders, *Phys. Lett. B* **772**, 210 (2017).
- [6] R. Franceschini, G. Panico, A. Pomarol, F. Riva, and A. Wulzer, Electroweak precision tests in high-energy diboson processes, *J. High Energy Phys.* **02** (2018) 111.
- [7] D. Liu and L.-T. Wang, Prospects for precision measurement of diboson processes in the semileptonic decay channel in future LHC runs, *Phys. Rev. D* **99**, 055001 (2019).
- [8] G. Panico, L. Ricci, and A. Wulzer, High-energy EFT probes with fully differential Drell-Yan measurements, *J. High Energy Phys.* **07** (2021) 086.
- [9] J. P. Delahaye, M. Diemoz, K. Long, B. Mansoulié, N. Pastrone, L. Rivkin, D. Schulte, A. Skrinsky, and A. Wulzer, Muon colliders, [arXiv:1901.06150](https://arxiv.org/abs/1901.06150).
- [10] D. Stratakis *et al.* (Muon Collider Collaboration), A muon collider facility for physics discovery, [arXiv:2203.08033](https://arxiv.org/abs/2203.08033).
- [11] M. Chiesa, F. Maltoni, L. Mantani, B. Mele, F. Piccinini, and X. Zhao, Measuring the quartic Higgs self-coupling at a multi-TeV muon collider, *J. High Energy Phys.* **09** (2020) 098.
- [12] A. Costantini, F. De Lillo, F. Maltoni, L. Mantani, O. Mattelaer, R. Ruiz, and X. Zhao, Vector boson fusion at multi-TeV muon colliders, *J. High Energy Phys.* **09** (2020) 080.
- [13] R. Capdevilla, D. Curtin, Y. Kahn, and G. Krnjaic, Discovering the physics of $(g-2)_\mu$ at future muon colliders, *Phys. Rev. D* **103**, 075028 (2021).
- [14] T. Han, Y. Ma, and K. Xie, High energy leptonic collisions and electroweak parton distribution functions, *Phys. Rev. D* **103**, L031301 (2021).
- [15] T. Han, D. Liu, I. Low, and X. Wang, Electroweak couplings of the Higgs boson at a multi-TeV muon collider, *Phys. Rev. D* **103**, 013002 (2021).
- [16] T. Han, Z. Liu, L.-T. Wang, and X. Wang, WIMPs at high energy muon colliders, *Phys. Rev. D* **103**, 075004 (2021).
- [17] D. Buttazzo and P. Paradisi, Probing the muon $g-2$ anomaly with the Higgs boson at a muon collider, *Phys. Rev. D* **104**, 075021 (2021).
- [18] W. Yin and M. Yamaguchi, Muon $g-2$ at a multi-TeV muon collider, *Phys. Rev. D* **106**, 033007 (2022).
- [19] D. Buttazzo, R. Franceschini, and A. Wulzer, Two paths towards precision at a very high energy lepton collider, *J. High Energy Phys.* **05** (2021) 219.
- [20] G.-y. Huang, F. S. Queiroz, and W. Rodejohann, Gauged $L_\mu - L_\tau$ at a muon collider, *Phys. Rev. D* **103**, 095005 (2021).
- [21] W. Liu and K.-P. Xie, Probing electroweak phase transition with multi-TeV muon colliders and gravitational waves, *J. High Energy Phys.* **04** (2021) 015.
- [22] R. Capdevilla, D. Curtin, Y. Kahn, and G. Krnjaic, No-lose theorem for discovering the new physics of $(g-2)_\mu$ at muon colliders, *Phys. Rev. D* **105**, 015028 (2022).
- [23] T. Han, S. Li, S. Su, W. Su, and Y. Wu, Heavy Higgs bosons in 2HDM at a muon collider, *Phys. Rev. D* **104**, 055029 (2021).
- [24] R. Capdevilla, F. Meloni, R. Simoniello, and J. Zurita, Hunting wino and higgsino dark matter at the muon collider with disappearing tracks, *J. High Energy Phys.* **06** (2021) 133.

- [25] T. Han, Y. Ma, and K. Xie, Quark and gluon contents of a lepton at high energies, *J. High Energy Phys.* **02** (2022) 154.
- [26] H. Al Ali *et al.*, The muon Smasher's guide, *Rep. Prog. Phys.* **85**, 084201 (2022).
- [27] P. Asadi, R. Capdevilla, C. Cesarotti, and S. Homiller, Searching for leptoquarks at future muon colliders, *J. High Energy Phys.* **10** (2021) 182.
- [28] S. Bottaro, D. Buttazzo, M. Costa, R. Franceschini, P. Panci, D. Redigolo, and L. Vittorio, Closing the window on WIMP dark matter, *Eur. Phys. J. C* **82**, 31 (2022).
- [29] S. Qian, C. Li, Q. Li, F. Meng, J. Xiao, T. Yang, M. Lu, and Z. You, Searching for heavy leptoquarks at a muon collider, *J. High Energy Phys.* **12** (2021) 047.
- [30] M. Chiesa, B. Mele, and F. Piccinini, Multi Higgs production via photon fusion at future multi-TeV muon colliders, [arXiv:2109.10109](https://arxiv.org/abs/2109.10109).
- [31] W. Liu, K.-P. Xie, and Z. Yi, Testing leptogenesis at the LHC and future muon colliders: A Z' scenario, *Phys. Rev. D* **105**, 095034 (2022).
- [32] J. Chen, T. Li, C.-T. Lu, Y. Wu, and C.-Y. Yao, Measurement of Higgs boson self-couplings through $2 \rightarrow 3$ vector bosons scattering in future muon colliders, *Phys. Rev. D* **105**, 053009 (2022).
- [33] S. Chen, A. Glioti, R. Rattazzi, L. Ricci, and A. Wulzer, Learning from radiation at a very high energy lepton collider, *J. High Energy Phys.* **05** (2022) 180.
- [34] C. Cesarotti, S. Homiller, R. K. Mishra, and M. Reece, Probing new gauge forces with a high-energy muon beam dump, *Phys. Rev. Lett.* **130**, 071803 (2023).
- [35] J. de Blas, J. Gu, and Z. Liu, Higgs boson precision measurements at a 125 GeV muon collider, *Phys. Rev. D* **106**, 073007 (2022).
- [36] Y. Bao, J. Fan, and L. Li, Electroweak ALP searches at a muon collider, *J. High Energy Phys.* **08** (2022) 276.
- [37] S. Homiller, Q. Lu, and M. Reece, Complementary signals of lepton flavor violation at a high-energy muon collider, *J. High Energy Phys.* **07** (2022) 036.
- [38] M. Forsslund and P. Meade, High precision Higgs from high energy muon colliders, *J. High Energy Phys.* **08** (2022) 185.
- [39] T. Han, D. Liu, I. Low, and X. Wang, Electroweak scattering at the muon shot, [arXiv:2312.07670](https://arxiv.org/abs/2312.07670).
- [40] D. Liu, L.-T. Wang, and K.-P. Xie, Composite resonances at a 10 TeV muon collider, [arXiv:2312.09117](https://arxiv.org/abs/2312.09117).
- [41] C. Csaki, A. Falkowski, and A. Weiler, The flavor of the composite pseudo-Goldstone Higgs, *J. High Energy Phys.* **09** (2008) 008.
- [42] B. Keren-Zur, P. Lodone, M. Nardecchia, D. Pappadopulo, R. Rattazzi, and L. Vecchi, On partial compositeness and the CP asymmetry in charm decays, *Nucl. Phys.* **B867**, 394 (2013).
- [43] S. Dawson, The effective W approximation, *Nucl. Phys.* **B249**, 42 (1985).
- [44] Z. Kunszt and D. E. Soper, On the validity of the effective W approximation, *Nucl. Phys.* **B296**, 253 (1988).
- [45] P. Borel, R. Franceschini, R. Rattazzi, and A. Wulzer, Probing the scattering of equivalent electroweak bosons, *J. High Energy Phys.* **06** (2012) 122.
- [46] D. Liu, A. Pomarol, R. Rattazzi, and F. Riva, Patterns of strong coupling for LHC searches, *J. High Energy Phys.* **11** (2016) 141.
- [47] A. Azatov, J. Elias-Miro, Y. Reymiujaji, and E. Venturini, Novel measurements of anomalous triple gauge couplings for the LHC, *J. High Energy Phys.* **10** (2017) 027.
- [48] G. Panico, F. Riva, and A. Wulzer, Diboson interference resurrection, *Phys. Lett. B* **776**, 473 (2018).
- [49] J. A. Dror, M. Farina, E. Salvioni, and J. Serra, Strong tW scattering at the LHC, *J. High Energy Phys.* **01** (2016) 071.
- [50] F. Maltoni, L. Mantani, and K. Mimasu, Top-quark electroweak interactions at high energy, *J. High Energy Phys.* **10** (2019) 004.
- [51] J. R. Andersen *et al.* (LHC Higgs Cross Section Working Group), Handbook of LHC Higgs cross sections: 3. Higgs properties, [arXiv:1307.1347](https://arxiv.org/abs/1307.1347).
- [52] H. Abramowicz *et al.* (CLICdp Collaboration), Top-quark physics at the CLIC electron-positron linear collider, *J. High Energy Phys.* **11** (2019) 003.
- [53] J. Alwall, R. Frederix, S. Frixione, V. Hirschi, F. Maltoni, O. Mattelaer, H. S. Shao, T. Stelzer, P. Torrielli, and M. Zaro, The automated computation of tree-level and next-to-leading order differential cross sections, and their matching to parton shower simulations, *J. High Energy Phys.* **07** (2014) 079.
- [54] R. Ruiz, A. Costantini, F. Maltoni, and O. Mattelaer, The effective vector boson approximation in high-energy muon collisions, *J. High Energy Phys.* **06** (2022) 114.
- [55] A. Falkowski, B. Fuks, K. Mawatari, K. Mimasu, F. Riva, and V. Sanz, Rosetta: An operator basis translator for standard model effective field theory, *Eur. Phys. J. C* **75**, 583 (2015).
- [56] P. A. Zyla *et al.* (Particle Data Group), Review of particle physics, *Prog. Theor. Exp. Phys.* **2020**, 083C01 (2020).
- [57] R. L. Workman *et al.* (Particle Data Group), Review of particle physics, *Prog. Theor. Exp. Phys.* **2022**, 083C01 (2022).
- [58] Z. Liu, K.-F. Lyu, I. Mahhub, and L.-T. Wang, Top Yukawa coupling determination at high energy muon collider, *Phys. Rev. D* **109**, 035021 (2024).
- [59] M. Cepeda *et al.*, Report from working group 2: Higgs physics at the HL-LHC and HE-LHC, *CERN Yellow Rep. Monogr.* **7**, 221 (2019).
- [60] M. L. Mangano, T. Plehn, P. Reimitz, T. Schell, and H.-S. Shao, Measuring the top Yukawa coupling at 100 TeV, *J. Phys. G* **43**, 035001 (2016).
- [61] K. Hagiwara, H. Yokoya, and Y.-J. Zheng, Probing the CP properties of top Yukawa coupling at an e^+e^- collider, *J. High Energy Phys.* **02** (2018) 180.
- [62] V. Barger, K. Hagiwara, and Y.-J. Zheng, CP-violating top-Higgs coupling in SMEFT, *Phys. Lett. B* **850**, 138547 (2024).
- [63] M. E. Cassidy, Z. Dong, K. Kong, I. M. Lewis, Y. Zhang, and Y.-J. Zheng, Probing the CP structure of the top quark Yukawa at the future muon collider, [arXiv:2311.07645](https://arxiv.org/abs/2311.07645).
- [64] J. Alwall, R. Frederix, S. Frixione, V. Hirschi, F. Maltoni, O. Mattelaer, H. S. Shao, T. Stelzer, P. Torrielli, and M. Zaro, The automated computation of tree-level and

- next-to-leading order differential cross sections, and their matching to parton shower simulations, *J. High Energy Phys.* **07** (2014) 079.
- [65] K. Hagiwara, R. D. Peccei, D. Zeppenfeld, and K. Hikasa, Probing the weak boson sector in $e^+e^- \rightarrow W^+W^-$, *Nucl. Phys.* **B282**, 253 (1987).
- [66] K. J. F. Gaemers and G. J. Gounaris, Polarization amplitudes for $e^+e^- \rightarrow W^+W^-$ and $e^+e^- \rightarrow ZZ$, *Z. Phys. C* **1**, 259 (1979).
- [67] G. F. Giudice, C. Grojean, A. Pomarol, and R. Rattazzi, The strongly-interacting light Higgs, *J. High Energy Phys.* **06** (2007) 045.